CrossMark

NuSTAR Observations of Four Mid-IR–Selected Dual AGN Candidates in Galaxy Mergers

Ryan W. Pfeifle[1,2,8] , Kimberly Weaver[1], Shobita Satyapal[3] , Claudio Ricci[3,4,5] , Nathan J. Secrest[6] , Mario Gliozzi[3] ,
Laura Blecha[7] , and Barry Rothberg[3,6]

[1] X-ray Astrophysics Laboratory, NASA Goddard Space Flight Center, Code 662, Greenbelt, MD 20771, USA; ryan.w.pfeifle@nasa.gov
[2] Oak Ridge Associated Universities, NASA NPP Program, Oak Ridge, TN 37831, USA
[3] Department of Physics and Astronomy, George Mason University, 4400 University Drive, MSN 3F3, Fairfax, VA 22030, USA
[4] Instituto de Estudios Astrofísicos, Facultad de Ingeniería y Ciencias, Universidad Diego Portales, Av. Ejército Libertador 441, Santiago, Chile
[5] Kavli Institute for Astronomy and Astrophysics, Peking University, Beijing 100871, People's Republic of China
[6] U.S. Naval Observatory, 3450 Massachusetts Avenue NW, Washington, DC 20392, USA
[7] Department of Physics, University of Florida, P.O. Box 118440, Gainesville, FL 32611-8440, USA
Received 2023 March 3; revised 2023 May 30; accepted 2023 June 27; published 2023 August 28

Abstract

Mergers of galaxies are a ubiquitous phenomenon in the universe and represent a natural consequence of the "bottom-up" mass accumulation and galaxy evolution cosmological paradigm. It is generally accepted that the peak of active galactic nucleus (AGN) accretion activity occurs at nuclear separations of $\lesssim 10$ kpc for major mergers. Here we present new NuSTAR and XMM-Newton observations for a subsample of mid-IR preselected dual AGN candidates in an effort to better constrain the column densities along the line of sight (LOS) for each system. Only one dual AGN candidate, J0841+0101, is detected as a single, unresolved source in the XMM-Newton and NuSTAR imaging, while the remaining three dual AGN candidates, J0122+0100, J1221+1137, and J1306+0735, are not detected with NuSTAR; if these nondetections are due to obscuration alone, these systems are consistent with being absorbed by column densities of $\log(N_H/cm^{-2}) \geqslant$ 24.9, 24.6, and 24.3, which are roughly consistent with previously inferred column densities in these merging systems. In the case of J0841+0101, the analysis of the 0.3–30 keV spectra reveal an LOS column density of $N_H \gtrsim 10^{24}$ cm^{-2}, significantly larger than the column densities previously reported for this system and demonstrating the importance of the higher signal-to-noise ratio XMM-Newton spectra and access to the >10 keV energies via NuSTAR. Though it is unclear if J0841 +0101 truly hosts a dual AGN, these results are in agreement with the high obscuring columns expected in AGNs in late-stage mergers.

Unified Astronomy Thesaurus concepts: AGN host galaxies (2017); Galaxy mergers (608)

1. Introduction

Over the last two and a half decades, we have come to understand that supermassive black holes (SMBHs) reside at the centers of most massive galaxies and that the masses of these SMBHs strongly correlate with the stellar velocity dispersions (M–σ; e.g., Ferrarese & Merritt 2000; Gebhardt et al. 2000) and luminosities (M–L; Gültekin et al. 2009) of their host spheroids. How these scaling relations between the SMBHs and their hosts are established remains an open debate, though one possible formation pathway is through the merging of galaxies, a ubiquitous phenomenon that is a key component of "bottom-up" mass accumulation and galaxy evolution. Gravitational tidal torques induced during a galaxy merger have been shown to drive large reservoirs of gas and dust into the galaxy nuclei (e.g., Barnes & Hernquist 1996), potentially fueling both star formation (e.g., Barnes & Hernquist 1991; Mihos & Hernquist 1996) and the central SMBHs (e.g., Hopkins et al. 2006, 2008); thus, mergers offer an efficient avenue for correlated stellar and SMBH growth. Numerous hydrodynamic simulations performed over the last decade also

agree that correlated SMBH growth—manifesting as dual active galactic nuclei (AGNs)—is expected to occur in late-stage mergers[9] with nuclear pair separations of <10 kpc and should coincide with the peak of the merger-induced SMBH growth (Van Wassenhove et al. 2012; Capelo et al. 2015, 2017; Blecha et al. 2018) while simultaneously being enshrouded by large columns of gas and dust (Capelo et al. 2017; Blecha et al. 2018). Observations agree well with these obscuration predictions; mergers have been shown to host higher fractions of obscured (and heavily obscured) AGNs compared to control samples (e.g., Satyapal et al. 2014; Kocevski et al. 2015; Ricci et al. 2017a, 2021; Koss et al. 2018; Lanzuisi et al. 2018), and the mid-infrared (mid-IR) AGN excess relative to optical AGNs increases as a function of decreasing nuclear pair separation, supporting the idea that obscuration increases in late-stage mergers (e.g., Satyapal et al. 2014). While only a few dozen dual AGNs have thus far been confirmed in the literature, a significant fraction of these systems show direct and indirect evidence for large absorbing columns on the order of $\gtrsim 10^{23}$–10^{24} cm^{-2} (e.g., Komossa et al. 2003; Bianchi et al. 2008; Piconcelli et al. 2010; Koss et al. 2016; De Rosa et al. 2018; Pfeifle et al. 2019a, 2019b). These high column densities may partially explain the lack of a larger population of known dual AGNs; dual AGN candidates are most often selected using

---

[8] NASA Postdoctoral Program Fellow.

---

[9] Note that dual AGNs can be found in earlier-stage mergers (e.g., Guainazzi et al. 2005; Koss et al. 2012; Blecha et al. 2018; De Rosa et al. 2018), but correlated growth is more likely in late-stage mergers.

optical spectroscopic diagnostics such as double-peaked emission lines (e.g., Wang et al. 2009; Liu et al. 2010; Smith et al. 2010; Comerford et al. 2011, 2012, 2015) but with relatively little success (Müller-Sánchez et al. 2015) or narrow spectroscopic emission line ratios (Liu et al. 2011; Guainazzi et al. 2021), but large absorbing columns along the line of sight (LOS) and/or high covering factors may bias against detecting large populations of dual AGNs in the optical band, resulting in fewer confirmed cases (see discussion in, e.g., Koss et al. 2012). Hydrodynamic simulations with radiative transfer postprocessing calculations performed in Blecha et al. (2018) demonstrated that this obscured phase of expeditious dual SMBH growth should be traced by the mid-IR colors of the merging system, where dual AGNs should exhibit Wide-Field Infrared Survey Explorer (WISE) mid-IR colors consistent with $W1 - W2 > 0.5$. Since the mid-IR colors trace the activity of the SMBHs regardless of the column density (and are therefore less sensitive to biases due to obscuration), mid-IR selection may offer a more statistically complete method of searching for and identifying dual AGNs.

Motivated by these recent theoretical results, we have been studying a sample of 15 late-stage galaxy mergers preselected with WISE (see Satyapal et al. 2017; Pfeifle et al. 2019a, 2019b). The sample selection methodology is thoroughly described in Satyapal et al. (2017) and Pfeifle et al. (2019b), but we briefly describe it here. We drew our sample from the Galaxy Zoo project (Lintott et al. 2008)[10] from the Sloan Digital Sky Survey (SDSS) DR7 (Abazajian et al. 2009), selecting only the systems that were most likely to be strongly disturbed mergers based upon the Galaxy Zoo classifications (weighted-merger-vote-fraction, $f_m > 0.4$; Darg et al. 2010). Cross-matching this sample with the AllWISE (Wright et al. 2019) release of the WISE catalog,[11] we required detections in the W1 and W2 bands with a signal-to-noise ratio of $>5\sigma$, and we applied the dual AGN mid-IR color criterion of $W1 - W2 > 0.5$ from Blecha et al. (2018). Visual inspection ensured the presence of two nuclei with projected separations of <10 kpc that were resolvable with Chandra. We list this sample of mid-IR–selected dual AGN candidates in Table 1 along with their redshifts, angular separations, and pair separations (see Table 1 in Pfeifle et al. 2019b, for additional details). There were two key questions we wished to address: (1) how effective is mid-IR selection in identifying dual AGNs in late-stage mergers, and (2) are dual AGNs in mid-IR–selected mergers indeed heavily obscured?

In Satyapal et al. (2017) and Pfeifle et al. (2019b), our follow-up Chandra X-ray observations revealed dual nuclear X-ray sources in 8/15 of the mid-IR–selected mergers. One of the targets that met our selection criteria and was included in our sample was Mrk 463, which actually hosts a known dual AGN system (Bianchi et al. 2008). Both direct (spectral analysis) and indirect diagnostics for absorption indicated that the AGNs in these mergers were indeed heavily obscured, with column densities $\gtrsim 10^{23}$–10^{24} cm^{-2}, in agreement with predictions from simulations (Capelo et al. 2017; Blecha et al. 2018). However, constraints on column densities and other AGN X-ray properties in heavily obscured AGNs can be difficult to obtain with softer-energy (<10 keV) X-ray telescopes alone without access to harder energies and specifically harder X-ray

---

[10] http://www.galaxyzoo.org
[11] http://wise2.ipac.caltech.edu/docs/release/allwise/

Table 1
WISE-selected Dual AGN Candidate Sample

Name (SDSS) (1)	z (2)	$\Delta\theta$ (arcsec) (3)	r_p (kpc) (4)	Class (5)
J012218.11+010025.7*	0.05546	8.7	8.7	DC
J084135.08+010156.2*	0.11060	3.9	7.9	DC
J084905.51+111447.2	0.07727	2.2 (a)	3.3 (a)	T
		4.0 (b)	5.8 (b)	T
J085953.33+131055.3	0.03083	16.1	9.9	S
J090547.34+374738.2	0.04751	6.2	5.8	S
J103631.88+022144.1	0.05040	2.8	2.8	S
J104518.03+351913.1	0.06758	7.0	9.0	DC
J112619.42+191329.3	0.10299	2.3	4.5	S
J114753.62+094552.0	0.09514	3.8 (c)	6.8 (c)	S
		2.4 (d)	4.3 (d)	S
J115930.29+532055.7	0.04498	2.7	2.4	S
J122104.98+113752.3*	0.06820	7.1	9.3	DC
J130125.26+291849.5	0.02340	21.8	10.3	DC
J130653.60+073518.1*	0.11111	2.0 (e)	4.0 (e)	DC
		3.7 (f)	7.4 (f)	DC
J135602.89+182218.2	0.05060	4.0	4.0	D
J235654.30–101605.3	0.07390	3.6	5.0	S

Notes. Basic information on the sample of 15 mid-IR–selected dual AGN candidates from Satyapal et al. (2017) and Pfeifle et al. (2019b). Column (1): SDSS target designation. Column (2): redshifts. Columns (3) and (4): angular separation of the galaxy nuclei in arcseconds and kiloparsecs, respectively. Column (5): classification following our analysis in Satyapal et al. (2017) and Pfeifle et al. (2019a, 2019b); we denote duals with (D), single AGNs with (S), and triple AGNs with (T), and we append (C) to the classification to indicate candidates. See Pfeifle et al. (2019b) for a full version of this table. Asterisks indicate objects studied in this work. (a) Angular separation between the SW and SE X-ray sources. (b) Angular separation between the SE and N X-ray sources. (c) Angular separation between the S and NE nuclei. (d) Angular separation between the S and NW nuclei. (e) Angular separation between the NE and SW X-ray sources. (f) Angular separation between the SW and SE X-ray sources.

spectral features, such as the Compton reflection hump beyond >10 keV. The Nuclear Spectroscopic Telescope Array (NuSTAR), on the other hand, offers access to energies beyond 10 keV (a half-power diameter of $58''$ and FWHM of $18''$; Harrison et al. 2013), and NuSTAR has been successful over the last decade in detecting large samples of obscured AGNs (e.g., Lansbury et al. 2017; Ricci et al. 2017b; Marchesi et al. 2018)—including heavily obscured AGNs in merging systems (e.g., Lansbury et al. 2017; Ricci et al. 2017a, 2021; Yamada et al. 2021)—and constraining their column densities and X-ray properties. In many cases, NuSTAR allowed for refined estimates of column densities derived from lower-quality and/or softer X-ray spectra (e.g., Lansbury et al. 2015; Marchesi et al. 2018). Therefore, the natural next step in our analysis of these heavily obscured dual AGNs and candidates was to study their hard X-ray properties as observed with NuSTAR.

Here we present new NuSTAR and XMM-Newton observations of a subsample of four mid-IR–selected dual AGN candidates drawn from Satyapal et al. (2017) and Pfeifle et al. (2019b), obtained in an effort to constrain the column densities in these potentially heavily obscured AGNs (marked with asterisks in Table 1). This work is organized as follows. In Section 2, we outline the new XMM-Newton and NuSTAR observations and detail our data processing steps. In Section 3, we describe our data analysis, and in Section 4, we report the

Table 2
New X-Ray Observations Examined in This Work

Name (1)	α (2)	δ (3)	Obs. Date (4)	ObsID (5)	Instrument (6)	Exp. (7)	Net Exp. (8)
J0122+0100	$01^h22^m21^s.0$	$+00°58^m39^s$	2018 Oct 26	60467001002	NuSTAR FPMA	32.4 ks	31.9 ks
J0122+0100	...	...	...	...	NuSTAR FPMB	32.4 ks	31.7 ks
J0841+0101	$08^h41^m45^s.3$	$+01°03^m06^s$	2018 Dec 29	60401002002	NuSTAR FPMA	48.4 ks	43.6 ks
J0841+0101	...	...	...	...	NuSTAR FPMB	48.4 ks	43.4 ks
J0841+0101	$08^h41^m35^s.04$	$+01°01'55''.2$	2018 May 10	0822470101	XMM EPIC PN	32 ks	28.7 ks
J0841+0101	...	...	...	...	XMM EPIC MOS1	32 ks	30.6 ks
J0841+0101	...	...	...	...	XMM EPIC MOS2	32 ks	30.6 ks
J1221+1137	$12^h20^m56^s.0$	$+11°36^m52^s$	2019 May 11	60467002002	NuSTAR FPMA	29.9 ks	27.5 ks
J1221+1137	...	...	...	...	NuSTAR FPMB	29.9 ks	28.8 ks
J1306+0735	$13^h06^m45^s.2$	$+07°34^m25^s$	2019 Jun 20	60467003002	NuSTAR FPMA	49.7 ks	49.6 ks
J1306+0735	...	...	...	...	NuSTAR FPMB	49.7 ks	49.3 ks

Note. Column (1): truncated merger designation. Columns (2) and (3): coordinates of X-ray observations. Columns (4) and (5): UT date of X-ray observations and observation ID. Column (6): facility and camera. Columns (7) and (8): effective exposure time after background flare filtering.

X-ray photometric and spectroscopic results. We discuss these results and their relation to the literature in Section 5, and we present our conclusions in Section 6. Throughout this work, we adopt the following cosmology: $H_0 = 70$ km s^{-1} Mpc^{-1}, $\Omega_M = 0.3$, and $\Omega_\Lambda = 0.7$.

2. Observations and Data Reduction

2.1. NuSTAR Observations

Pointed observations of J0122+0100, J1221+1137, and J1306+0735 were obtained with NuSTAR between 2018 October 26 and 2019 June 20 (Program ID 04185), while J0841+0101 was observed by NuSTAR on 2018 May 10 (Program 082247). The former three mergers were targeted as part of a NuSTAR follow-up program[12] for the four dual AGN candidates in our pilot program (Satyapal et al. 2017); J1045+3519 was included in that proposal but unfortunately not awarded time. On the other hand, J0841+0101 was targeted in a separate, joint XMM-Newton/NuSTAR follow-up study[13] aimed at confirming the reported Fe Kα (Pfeifle et al. 2019b) and placing more stringent constraints on the column density. The observations were conducted with the targets at the aimpoint, with total exposure times ranging from 29.9 to 49.7 ks. Details of the observations are shown in Table 2. Observations of three other mergers in our sample, J0849+1114, J1301+2911 (NGC 4922), and J1356+1822 (Mrk 463), were previously published and studied by Pfeifle et al. (2019a), Ricci et al. (2017a), and Yamada et al. (2018), respectively; rather than reanalyzing these systems, we refer to the results of these previous works where relevant in this work. The NuSTAR observations were processed using the NuSTAR Data Analysis Software (NUSTARDAS; Perri et al. 2021)[14] v0.4.7 package available in HEASOFT v6.27 (NASA High Energy Astrophysics Science Archive Research Center 2014),

along with the latest CALDB version and the clock correction file at the time of reprocessing. Level two data products were created using NUPIPELINE (v0.4.7), and specific processing choices to account for the South Atlantic Anomaly were made based upon the provided background light curves for focal plane modules A and B (FPMA and FPMB); the TENTACLE YES option was used in cases where the background was not stable over the duration of the observation (per the NUSTAR-DAS manual). The DMCOPY tool contained within the Chandra Interactive Analysis of Observations (CIAO) software package (Fruscione et al. 2006) was used to create energy-filtered images for the 3–10 keV (soft), 10–24 keV (hard), and 3–24 keV (full) NuSTAR energy bands. As discussed in Section 3, counts for specific energy bands were extracted from these energy-filtered science images. Where spectral extraction was relevant, we used the NUPRODUCTS script to extract the stage 3 data products using the source and background regions described in Section 3.1.1, yielding source and background spectra, as well as the relevant response files extracted across the 3.0–78.0 keV energy range. We grouped the FPMA and FPMB spectra by 1 count bin^{-1} using the HEASOFT GRPPHA command in order to fit the spectra in XSPEC using Cash statistics (Cash 1979), which is more appropriate than χ^2 statistics given the low number of counts within the spectra.

2.2. XMM-Newton Observations

On 2018 May 10, J0841+0101 was observed on-axis by XMM-Newton (HEW: ∼17″) for a total of 32 ks (see Table 2 for details). We reprocessed the observation using SAS v20.0.0, cleaning the event files of bad pixels, bad patterns, and background flares. We generated energy-filtered science images for each of the EPIC cameras using the SAS EVSELECT command. Source spectra were generated using the EVSELECT command using a 30″ radius source aperture and a 1′ radius background aperture (placed in a source-free region on the same CCD); response files were generated using the RMFGEN and ARFGEN commands. We grouped the spectra using GRPPHA at 1 count bin^{-1} in order to use Cash statistics (Cash 1979) during spectral fitting in XSPEC.

2.3. Chandra Observations

In addition to the NuSTAR and XMM-Newton observations of J0841+0101, we also retrieved the archival Chandra ACIS-S

---

[12] For these observations, we estimated the intrinsic AGN 2–10 keV luminosities by converting the 6 μm luminosity (derived from WISE) to the 2–10 keV luminosity via the Stern (2015) relation. We used these intrinsic X-ray luminosities along with the NuSTAR responses to simulate fake spectra using MYTORUS and gauge the required exposure times needed for 400–900 counts.

[13] For this joint observation, we used the combined count rates found by Chandra to determine the count rates for XMM via PIMMS, assuming heavy absorption, and to generate fake NuSTAR spectra comprising several hundred counts using the NuSTAR responses.

[14] https://heasarc.gsfc.nasa.gov/docs/nustar/analysis/

observations for use during the spectral analysis. J0841+0101 was observed for 20 ks on 2012 February 25 and 23 ks on 2016 January 10, and these observations were examined and published by Comerford et al. (2015), Pfeifle et al. (2019b), and Foord et al. (2020). We reprocessed the observations using CIAO v.4.14 and CALDB v.4.9.7 using the CHANDRA_REPRO script. Energy-filtered images were again created using DMCOPY within CIAO. Spectra were extracted using the SPECEXTRACT script, and we used the 1″5 source and associated background aperture choices from Pfeifle et al. (2019b) to extract the source and background spectra. As in the case of the NuSTAR and XMM-Newton data, the spectra were grouped by 1 count bin^{-1}.

3. Data Analysis

3.1. X-Ray Photometric Analysis

3.1.1. Source Detection and Photometry

The NuSTAR and XMM-Newton source aperture positions were chosen using the WAVDETECT tool within the CIAO package (Fruscione et al. 2006) and the "centroid" feature in DS9 when necessary; for nondetected systems, we placed apertures at the SDSS positions of the galaxy merger. Source apertures 45″ in radius (∼64% enclosed energy fraction; EEF) were used to extract NuSTAR spectra, and counts for each source with background annuli of inner radius 90″ and outer radius 150″ were used to extract background spectra and counts. An inner radius of 90″ ensures minimal contribution from the source. The effective area of NuSTAR drops off dramatically after 24–30 keV, hindering the utility of the higher energy bands; we limit our photometric investigation to the 3–24 keV energy range for the NuSTAR data, although for the spectroscopic investigation of J0841+0101, we use the 3.0–30 keV range for the NuSTAR data.

For NuSTAR, we extracted counts from the energy-filtered images using the DMEXTRACT package within CIAO. We assumed Gaussian statistics in the case of detected sources with greater than 20 counts, computing the source error as $\sqrt{N}$ (where N is the number of counts), and generated background-subtracted counts after normalizing the background counts to the size of the source region. We derived formal statistical significance levels using the background-subtracted counts and required a significance threshold of 3σ for a source to be considered formally detected within a particular energy band. As an additional check, the logarithm of the binomial no-source probability (Lansbury et al. 2014) was computed for each system, which can be particularly important for identifying weak sources that do not necessarily meet formal detection thresholds. The minimum threshold for the no-source statistic is $\log(P_B) \leqslant -2.7$, meaning that if $\log(P_B) \leqslant -2.7$, the gross counts within an aperture are unlikely to be purely the result of a background fluctuation. For instances of nondetections in the NuSTAR imaging, we instead computed the 3σ (99.7% confidence level) upper limits for the net source counts following the Bayesian method of Kraft et al. (1991), which takes into account the gross measured counts in the source and background regions.

Table 3 shows the FPMA and FPMB background-subtracted photometry for all of the dual AGN candidates observed by NuSTAR; no correction for the encircled energy fraction was made to these net counts. J0122+0100, J1221+1137, and J1306+0735 were not formally detected or identified using the

binomial source statistic in the NuSTAR imaging, J0841+0101 was clearly detected by both NuSTAR and XMM-Newton.

3.1.2. NuSTAR Flux Calculations

For each of the nondetected dual AGN candidates observed by NuSTAR, we converted the observed count rates to observed fluxes (or flux upper limits) in each of the 3–24, 3–10, 10–24, and 2–10 keV energy bands (in order to directly compare to our previous work with Chandra; i.e., Pfeifle et al. 2019a) using the Chandra PIMMS toolkit. To accomplish this, we combined the count rates from FPMA and FPMB for each energy band and then scaled the combined count rates to what would have been derived from an aperture enclosing 50% of the enclosed energy, as required before inputting the count rates into PIMMS. When calculating fluxes, we assumed a simple power law with $\Gamma = 1.8$ (e.g., Mushotzky et al. 1993; Ricci et al. 2017b), and we provided PIMMS the EEF-scaled fluxes, the SDSS spectroscopic redshifts of the merging systems, and the Galactic N_H along the LOS, which we retrieved from the Swift Galactic N_H calculator.[15] The resulting fluxes are tabulated in Table 4. Note that for the case of J0841+0101, we performed detailed spectral fitting and therefore did not need to perform this simple count rate–to–flux conversion.

3.1.3. Indirect Column Density Estimation

As mentioned in Section 3.1.1 and discussed in Section 4.1, J0122+0100, J1221+1137, and J1306+0735 were not detected by NuSTAR, hindering our ability to constrain the column densities along the LOS. To circumvent this issue, we indirectly derived lower limits on the column density for each of these dual AGN candidates by comparing the ratio of the hard X-ray flux upper limits and the expected unobscured hard X-ray fluxes ($F_{10-24\,\mathrm{keV,upper\,limit}}/F_{10-24\,\mathrm{keV,expected}}$) to sets of attenuation curves (e.g., Ricci et al. 2015) generated in XSPEC. This technique was used in Pfeifle et al. (2023), and we briefly describe the process here.

1. We began by calculating the hard X-ray 10–24 keV flux upper limit for each dual AGN candidate as described in Section 3.1.2.
2. Then, we calculated the expected intrinsic hard X-ray fluxes. We estimated the expected 2–10 keV flux using the Asmus et al. (2015) relation between the 2–10 keV and 12 μm fluxes, where we used the AGN 12 μm flux derived from our latest spectral energy distribution (SED) fitting, which we describe in Appendix A. With the expected intrinsic 2–10 keV flux in hand, we then converted this to the 10–24 keV flux using a scale factor derived from a power-law model in XSPEC assuming $\Gamma = 1.8$.
3. We then took the ratio between the 10–24 keV flux upper limit from NuSTAR and the expected 10–24 keV flux.
4. Next, we established an attenuation curve for each merger system. This was generated with a model in XSPEC that includes a primary power law, photoelectric absorption, Compton scattering, reprocessed emission from a torus, and Thomson scattering, expressed in XSPEC as (f × cutoffpl) + (tbabs × cabs × cutoffpl) + Borus. This model assumed $\Gamma = 1.8$ (Mushotzky et al. 1993; Ricci et al. 2017b) and a scattering fraction of 0.05% ($f = 0.005$), and the model was

---

[15] https://www.swift.ac.uk/analysis/nhtot/

Table 3
NuSTAR Photometry

System	FPM	α	δ	z	Net Counts		
					3–24 keV	3–10 keV	10–24 keV
(1)	(2)	(3)	(4)	(5)	(6)	(7)	(8)
J0122+0100	A	$1^h22^m17^s839$	$+1°00^m30^s336$	0.05546	<24.3	<21.0	<17.0
	B	$1^h22^m17^s839$	$+1°00^m30^s336$	0.05546	<50.6	<30.7	<35.8
J0841+0101	A	$8^h41^m34^s879$	$+1°02^m03^s041$	0.11060	296.7 ± 23.9	151.2 ± 17.2	148.9 ± 16.6
	B	$8^h41^m35^s306$	$+1°01^m54^s559$	0.11060	331.5 ± 25.4	176.3 ± 19.2	154.5 ± 16.7
J1221+1137	A	$12^h21^m04^s845$	$11°37^m53^s570$	0.06820	<22.5	<20.2	<16.1
	B	$12^h21^m04^s845$	$11°37^m53^s570$	0.06820	<37.6	<30.3	<25.4
J1306+0735	A	$13^h06^m53^s601$	$+7°35^m18^s850$	0.11111	<33.8	<32.6	<20.0
	B	$13^h06^m53^s601$	$+7°35^m18^s850$	0.11111	<31.7	<33.6	<17.7

Notes. NuSTAR photometry for the 3–24 keV (full), 3–10 keV (soft), and 10–24 keV (hard) energy bands. Columns (1) and (2): system name and FPM. Columns (3)–(5): R.A., decl., and redshift. Columns (6)–(8): full, soft, and hard band counts. No correction was made for the enclosed energy fraction in this table.

stepped through column densities of $\log(N_H/\mathrm{cm}^{-2}) =$ 22–25.4 in increments of $\Delta \log(N_H/\mathrm{cm}^{-2}) = 0.2$ in order to build the attenuation curve as a function of column density. During this step, we built two curves per system, one for each choice of covering factor: $C = 0.5$ and 0.99, where 0.99 may be more appropriate in merging systems where the obscuring material may take up a large fraction of the sky as seen by the AGN (Ricci et al. 2017a, 2021; Yamada et al. 2021). These curves were normalized by the "intrinsic" 10–24 keV flux of the model measured when $\log(N_H/\mathrm{cm}^{-2}) = 22.0$.

Once the attenuation curves were generated for each merger and the ratio of $F_{10-24\,\mathrm{keV,upper\ limit}}/F_{10-24\,\mathrm{keV,expected}}$ was known, we interpolated the flux ratio between values in the attenuation curves to derive the column densities required for the observed X-ray suppression. We list the derived column densities in Table 4 alongside the NuSTAR fluxes derived in Section 3.1.2.

3.2. Spectroscopic Analysis

The only source formally detected by NuSTAR with statistical significance was J0841+0101, and here we have used the new NuSTAR and XMM-Newton observations in conjunction with the archival Chandra observations to study the X-ray spectral properties in the 0.1–30 keV band. We limited our analysis to the 0.1–30 keV energy band due to the drop in the effective area of NuSTAR beyond ~30 keV. As we moved from simpler to more complex models, for each spectral model component with one free parameter (introducing one new degree of freedom), the C-stat value for the fit was required to change such that $\mathrm{Cstat_{old}} - \mathrm{Cstat_{new}} > 2.71$ to be considered a statistically significant improvement to the fit (e.g., Tozzi et al. 2006; Brightman et al. 2014), and each new spectral model was visually inspected to ensure that a proper fit had been found.

We began our fitting process with a simple phenomenological power-law model that accounts for Galactic N_H and includes photoelectric absorption, Compton scattering, and Thompson scattering (in the form of a scattered power law), given in XSPEC as TBABS×(F×CUTOFFPL+TBABS×CABS× CUTOFFPL).

The normalization and photon index of the scattered component were tied to that of the intrinsic power law. Residuals leftover after this initial fit suggested the presence of

two thermal components in the 0.1–1 keV band, which we modeled with two separate APEC components; iteratively adding and fitting the spectra with these additional components yielded ΔC-stat = 81.8 and 33.1. To account for excess emission above 10 keV, we included a reflection component off of a cold slab, described by the PEXRAV model in Xspec (ΔC-stat = 18.5); we set $R < 0$ so that this component represented only a reflection component and did not include an intrinsic power-law component. We assumed solar abundances and an inclination angle of 60° for each fit; these parameters were not free to vary. Finally, strong excess emission was observed near 6.4 keV (in the source rest-frame), indicative of an Fe $K\alpha$ emission line (originally identified by Pfeifle et al. 2019b, using Chandra X-ray observations); we modeled this emission using a Gaussian line (ZGAUSS) with the line centroid fixed to 6.4 keV and the width fixed to 0.01 keV to model only the narrow component of the line (ΔC-stat = 20.9). The best-fitting phenomenological model is given in XSPEC as TBABS×(APEC+APEC+F×CUTOFFPL+ ZTBABS×CABS×CUTOFFPL+PEXRAV+ZGAUSS).

We followed this procedure again but this time employed the physically motivated and self-consistent torus model, BORUS (Baloković et al. 2018), to account for reprocessing of the intrinsic AGN emission by an obscuring torus instead of using a PEXRAV component. There is an important distinction between the phenomenological model and this physically motivated model: BORUS provides a parameter for the torus column density, which can be different than the LOS column density. For simplicity, we began the fitting process using a model that accounts for the torus column density, an absorbed power law (with an LOS column density tied to that of the torus column density for a simpler geometric case) that accounts for photoelectric absorption and Compton scattering, as well as Thompson scattering, given in XSPEC as TBABS×(F× CUTOFFPL+ZTBABS×CABS×CUTOFFPL +BORUS). We assume solar abundances, a torus half-opening angle of 60° (corresponding to a covering factor of 50%), and an inclination angle of 70° for each fit; these parameters were not free to vary. We also tied the power-law photon indices and normalizations of the power-law models and the BORUS model together. As in the case of the phenomenological model, we found that the addition of two APEC components (ΔC-stat = 61.8 and 34.8) statistically and visually improved the fit. Furthermore, we found that untying the LOS and torus column densities resulted in a statistically significant improvement to the fit (ΔC-stat = 11.7). The final best-fitting model for this

Table 4
X-Ray Properties for the NuSTAR Nondetected AGNs

System	NuSTAR Observed Flux (10^{-13} erg cm^{-2} s^{-1})				Chandra Flux (10^{-13} erg cm^{-2} s^{-1})	Covering Factor	$\log(N_{\rm H}/{\rm cm}^{-2})$
	3–24 keV	3–10 keV	10–24 keV	2–10 keV	2–10 keV		
(1)	(2)	(3)	(4)	(5)	(6)	(7)	(8)
J0122+0100	<0.895	<0.434	<1.19	<0.558	0.14 ± 0.02	0.5 (0.99)	>24.7 (>24.9)
J1221+1137	<1.81	<1.07	<2.36	<1.37	0.08 ± 0.03	0.5 (0.99)	>24.4 (>24.6)
J1306+0735	<1.13	<0.80	<1.23	<1.03	0.08 ± 0.01	0.5 (0.99)	>24.1 (>24.3)

Note. NuSTAR fluxes (or flux upper limits) derived using PIMMS assuming a power-law index of $\Gamma = 1.8$ for the 3–24, 3–10, 10–24, and 2–10 keV energy bands. Column (1): system name. Columns (2)–(5): fluxes for the 3–24, 3–10, 10–24, and 2–10 keV energy bands. Column (6): observed 2–10 keV flux from Pfeifle et al. (2019b), where the values reported here are the sums of the X-ray fluxes of the nuclei in each merger. Column (7): choice of covering factor (see Section 3.1.3). Column (8): column density lower limits derived using the attenuation curves and flux ratios described in Section 3.1.3. The values in parentheses are calculated assuming a covering factor of 0.99 rather than 0.5. Note that we do not provide a column density lower limit for J0841+0101 because we were able to fit the spectra for that system.

physically motivated case was given by TBABS×(APEC+APEC +F×CUTOFFPL+ZTBABS×CABS×CUTOFFPL+BORUS). BORUS self-consistently models the Fe Kα emission line, so there was no need to include a Gaussian emission line component in the model.

Throughout the fitting process, we froze the redshift to the spectroscopic redshift given by SDSS and the Galactic $N_{\rm H}$ to that given by the Swift Galactic $N_{\rm H}$ calculator (Willingale et al. 2013). A multiplicative constant was added to each model and left free to vary within ±30% of the first data instance loaded into XSPEC to account for interdetector sensitivity; during the fitting process, these constants were monitored to ensure that they did not vary by more than roughly ±15% (all but one constant remained <10%).

4. Results

4.1. Photometric Results

Of the four newly imaged dual AGN candidates, three (J0122+0100, J1221+1137, and J1306+0735) were not detected by NuSTAR ($<3\sigma$), and the binomial no-source statistics were inconclusive. The source positions and upper limits on the counts for these three systems are reported in Table 3. On the contrary, J0841+0101 was well detected by Chandra, XMM-Newton, and NuSTAR in every energy band explored, and the counts from the NuSTAR observation are reported in Table 3. We show the SDSS r-band image and NuSTAR 3–10, 10–24, and 3–24 keV imaging for each of these four mergers in Figure 1. Using the count rates and upper limits, we calculated the 3–24, 3–10, 10–24, and 2–10 keV fluxes and flux upper limits for all four of the newly observed systems, assuming a power-law index of $\Gamma = 1.8$ (see Section 3.1.2). The nondetections in J0122+0100, J1221 +1137, and J1306+0735 suggest that there are no 10–24 keV X-ray-emitting AGNs in excess of 1.19×10^{-13}, 2.36×10^{-13}, and 1.23×10^{-13} erg s^{-1} cm^{-2}, respectively, in these systems.

To offer a direct comparison to our previous work with Chandra, we tabulated the 2–10 keV fluxes derived from NuSTAR in Table 4. The previous Chandra observations provided far more stringent measurements of the 2–10 keV fluxes in these mergers ($\approx 1.4 \times 10^{-14}$ erg cm^{-2} s^{-1} for J0122 +0100, $\approx 8.4 \times 10^{-15}$ erg cm^{-2} s^{-1} for J1221+1137, and $\approx 7.5 \times 10^{-15}$ erg cm^{-2} s^{-1} for J1306+0735; Pfeifle et al. 2019b); in each of the three nondetection cases presented here,

the 2–10 keV flux upper limits derived from NuSTAR are well in excess of the measured 2–10 keV fluxes reported in Pfeifle et al. (2019b), so it is not surprising that the mergers remained undetected in the softer 3–10 keV NuSTAR energy band. To better illustrate this point, we display the intrinsic AGN 12 μm luminosities (derived via SED fitting; see Appendix A) and the 2–10 keV luminosities derived via Chandra and NuSTAR for the subsample examined here in Figure 2 along with the Chandra 2–10 keV luminosities for the remainder of the sample (from Pfeifle et al. 2019b). We also list the observed NuSTAR 3–24, 3–10, 10–24 keV, and 2–10 keV luminosities for the nondetected sources in Table 5 alongside the combined, observed Chandra 2-10 keV luminosity for each merger (from Pfeifle et al. 2019b).

Without spectra for J0122+0100, J1221+1137, and J1306 +0735, we indirectly estimated lower limits on the column densities along the LOS as outlined in Section 3.1.3. The 10–24 keV flux upper limits derived from NuSTAR imply column densities of $\log(N_{\rm H}/{\rm cm}^{-2}) \geqslant 24.9$, 24.6, and 24.3 (assuming a covering factor of $C = 0.99$), respectively, assuming the nondetection in the 10–24 keV band is due purely to obscuration. These column density lower limits are roughly consistent with what we found in Pfeifle et al. (2019b), where the differences are likely due to the different methods used to estimate the column densities.

4.2. Spectroscopic Results

Our broadband (0.1–30 keV) joint NuSTAR, XMM-Newton, and Chandra spectroscopic analysis for J0841+0101 yielded direct constraints on the AGN X-ray properties. In Table 6, we present the parameters for our two best-fitting models, described in Section 3.2: one phenomenological model, which we refer to as the PEXRAV model, and one physical torus model, which we refer to as the BORUS model. These best-fitting models are shown in Figure 3. Each of these best-fitting models features two thermal components in the 0.1–1 keV band ($T_1 = 0.17^{+0.03}_{-0.06}$ and $T_2 = 0.90^{+0.13}_{-0.11}$ keV for the PEXRAV model and $T_1 = 0.16^{+0.04}_{-0.06}$ and $T_2 = 0.90^{+0.14}_{-0.12}$ keV for the BORUS model), scattered emission ($f = 2.7^{+16.1}_{-2.2}\%$ and $0.7^{+0.4}_{-0.3}\%$), photon indices typical of Seyfert 2 AGNs ($1.9^{+0.3}_{-0.3}$ for the PEXRAV model and $2.0^{+0.2}_{-0.2}$ for the BORUS model), components for reflection and reprocessing ($R = -2.3^{+1.6}_{-6.9}$ for the PEXRAV model), iron Kα fluorescent emission lines (equivalent width of 0.3 keV in the case of the PEXRAV
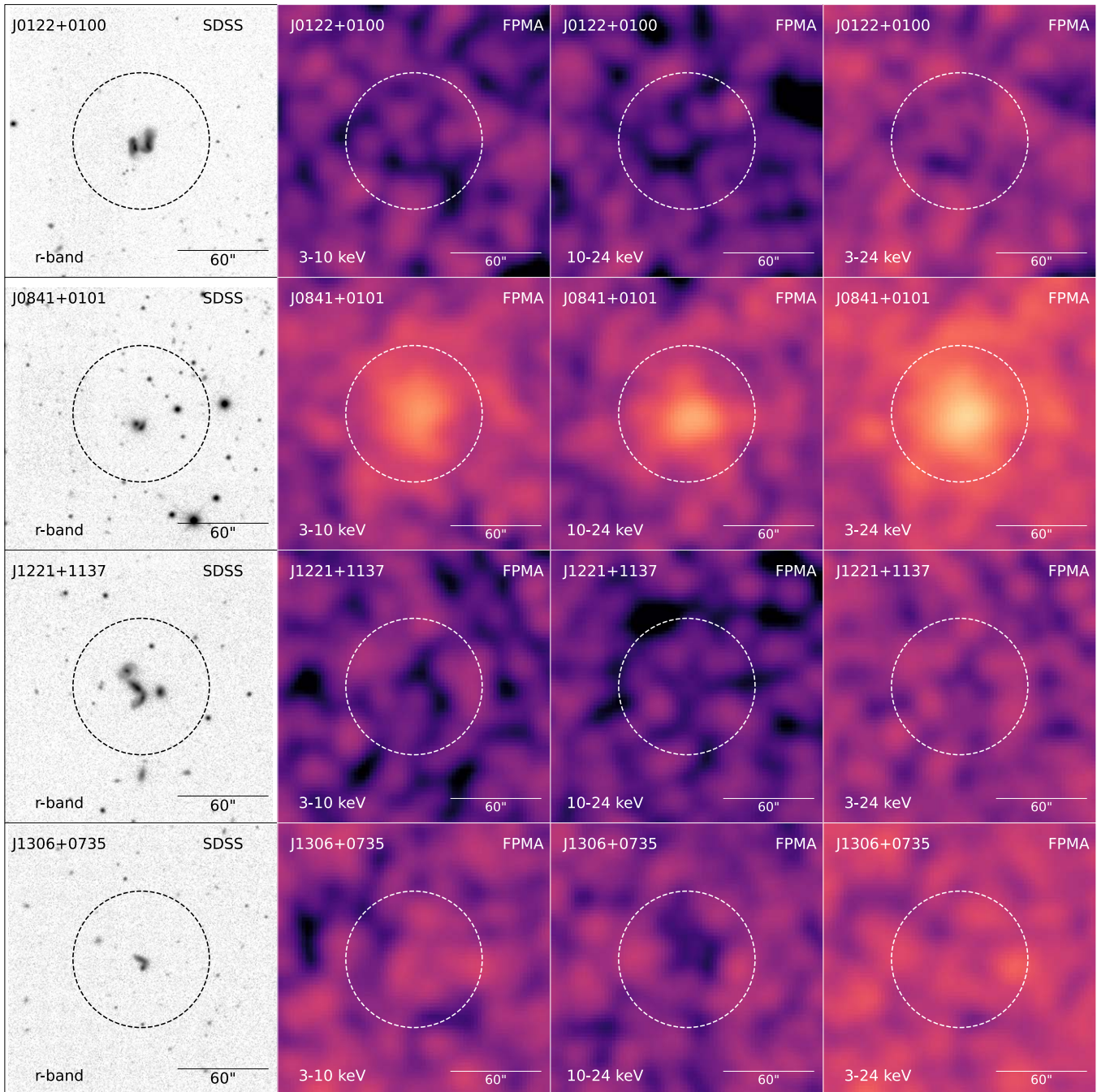
Figure 1. The SDSS *r*-band and NuSTAR FPMA imaging for (top to bottom) J0122+0100, J0841+0101, J1221+1137, and J1306+0735. Left to right: SDSS *r*-band and NuSTAR FPMA 3–10, 10–24, and 3–24 keV bands. We smoothed the X-ray images with a 3 pixel Gaussian kernel and used the perceptually uniform sequential color map "magma" in MATPLOTLIB. Dashed 45″ radius circles represent the source extraction regions. The scale bar in the bottom right corner of each panel indicates an angular size of 60″.

model), and LOS absorption. The key difference between these models is how the LOS obscuration is handled; for the BORUS model, we allow the torus column density to vary independently of the LOS obscuration, and the best-fitting model finds different column densities for each: a torus average column density (given in log units, as provided by the model) of $\log(N_{\mathrm{H}}/\mathrm{cm}^{-2}) = 23.0^{0.1}_{-0.1}$ and an LOS column density of $N_{\mathrm{H}} = 121^{+20}_{-18} \times 10^{22}\,\mathrm{cm}^{-2}$. The PEXRAV model, on the other hand, allowed for only a single column density along the LOS, which yielded $N_{\mathrm{H}} = 80.1^{+44.9}_{-52.8} \times 10^{22}\,\mathrm{cm}^{-2}$; nonetheless, the column density derived using the PEXRAV model is consistent with the

LOS column density derived using the BORUS model within the quoted error bounds. The observed and absorption corrected NuSTAR 2–10 and 3–24 keV fluxes and luminosities derived from these models are given in Table 7.

These column densities are higher than those derived using the Chandra data alone in Pfeifle et al. (2019b), though there is significant overlap when considering the error bounds in Table 6; specifically, the LOS column density of the PEXRAV model is consistent within the error bounds with that found in Pfeifle et al. (2019b), while the torus column density of the BORUS model is slightly smaller than what was found in
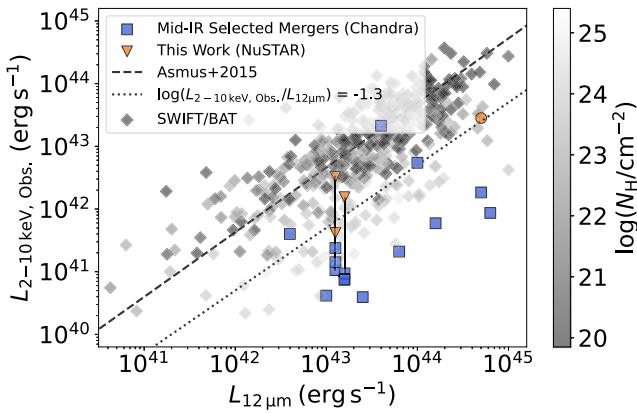
Figure 2. Comparing the intrinsic AGN 12 μm luminosity to the total observed 2–10 keV luminosity. The intrinsic AGN 12 μm luminosity (derived via SED fitting) is given on the abscissa, and the total observed 2–10 keV luminosity is given on the ordinate. Mid-IR–selected mergers from Satyapal et al. (2017) and Pfeifle et al. (2019b) are shown as blue squares; mergers examined in this work with NuSTAR that hence have 2–10 keV luminosities derived from NuSTAR are shown in orange, where inverted triangles indicate upper limits, and the circle indicates J0841+0101, the only source detected by NuSTAR. Vertical lines connect sources observed with Chandra and NuSTAR. For comparison, we underlay the observed 2–10 keV X-ray and intrinsic AGN 12 μm luminosities from the Swift-BAT sample drawn from Ricci et al. (2017b) and Ichikawa et al. (2017, 2019); the column densities of the Swift-BAT sample are displayed through the auxiliary color map. The dashed line indicates the expected relation for unobscured AGNs from Asmus et al. (2015), while the dotted line indicates the ratio at which we expect the AGNs to be heavily obscured (Pfeifle et al. 2022).

Pfeifle et al. (2019b). Nonetheless, the LOS column density found with the BORUS model does imply a significantly higher column density than was previously reported. The power-law index values found in this work are better constrained than with the Chandra data alone in Pfeifle et al. (2019b), but the scattered fractions determined here are consistent with the values found in Pfeifle et al. (2019b). We also confirm the presence of the iron Fe Kα line previously reported in Pfeifle et al. (2019b), though with a smaller equivalent width ($0.26^{+0.15}_{-0.07}$ versus 0.75 keV in Pfeifle et al. 2019b). The refinement of the X-ray properties in this work relative to previous works is not surprising; the addition of the XMM-Newton spectra with a higher signal-to-noise ratio in the 0.1–10 keV band in concert with access to the hard-energy 3–30 keV band via NuSTAR yielded better constraints on the AGN X-ray properties.

The analysis presented here comes with a clear caveat: we assume that there is only a single hard X-ray-emitting AGN in this merging system. In reality, if the second galaxy hosts a heavily Compton-thick AGN that emits strongly in the hard X-rays, this AGN would contribute appreciably to the observed hard X-ray spectrum; thus, the derived X-ray spectral properties would describe the sum of the spectra of the two sources rather than the specific properties attributable to one AGN or the other. At the present time, the spectra are not of sufficient quality to attempt such a deconvolution. While the spectroscopic analysis here does not provide evidence for or against the dual AGN scenario for J0841+0101 (it is unclear if this is a dual AGN; see Foord et al. 2020, who found that the system is consistent with a single X-ray-emitting AGN using the BAYMAX tool), it nonetheless represents a clear case of heavy absorption induced by a merger. Our X-ray spectroscopic results showing the presence of a strong soft X-ray emission component are consistent with the analysis presented

in Foord et al. (2020), who concluded that J0841+0101 comprises a single resolved X-ray source surrounded by diffuse and extended emission.

5. Discussion

5.1. Heavily Obscured AGNs or X-Ray Underluminous LIRGs?

Though NuSTAR could only provide constraints on the nuclear column density in one of the four dual AGN candidates examined here, mid-IR–selected dual AGNs are nonetheless expected to be heavily obscured (e.g., Blecha et al. 2018), and this has been observed here for J0841+0101 ($N_H \approx 80$–100×10^{22} cm^{-2}), as well as for other AGNs from our mid-IR–selected sample: J0849+1114 in Pfeifle et al. (2019a), Mrk 463 (Bianchi et al. 2008; Yamada et al. 2018; Pfeifle et al. 2019b), NGC 4922 (Ricci et al. 2017a; Pfeifle et al. 2019b), and J0859+1310 (Pfeifle et al. 2019b). If J0122+0100, J1221+1137, J1306+0735, and the other remaining mergers from our mid-IR sample (e.g., Satyapal et al. 2017; Pfeifle et al. 2019b) follow this trend, we should expect nearly all of these systems to host heavily obscured AGNs, as was inferred from the comparison between their observed X-ray luminosities and WISE 12 μm luminosities (see Figure 8 from Pfeifle et al. 2019b) and shown here in Figure 2. While the 12 μm luminosities differ from those shown in our previous work,[16] Figure 2 once again shows that the majority of our sample of mid-IR–selected dual AGN candidates display substantial X-ray deficits relative to their 12 μm luminosities, suggesting the presence of large column densities in these systems. The upper limits derived for J0122+0100, J1221+1137, and J1306+0735 clearly exceed those derived from Chandra; while the Chandra flux levels indicate that the AGNs in these systems are likely to be obscured, they are likely not as obscured as indicated by the NuSTAR flux upper limits in this work.

The observed X-ray deficits relative to the mid-IR luminosities observed for J0122+0100, J1221+1137, and J1306+0735 (and other mergers in our sample) may not come as a surprise, given the fact that these mergers are all classified as luminous infrared galaxies (LIRGs) based on their infrared luminosities, i.e., $\log(L_{8-1000\,\mu m}/L_\odot) > 11$; LIRGs are in fact known to be underluminous in X-rays relative to the infrared luminosity (Iwasawa et al. 2011; Torres-Albà et al. 2018), regardless of whether they host an AGN. Obscuration is often implicated as the source for the observed X-ray deficits in LIRGs that host AGNs; the presence of heavily obscured AGNs in these mergers is therefore consistent with the general picture that LIRGs are associated with high concentrations of gas and dust and that AGNs identified in late-stage LIRG mergers are often heavily obscured (Ricci et al. 2017a, 2021), some of these AGNs have also lacked detections in hard X-ray NuSTAR imaging (Ricci et al. 2017a, 2021). However, the characteristic LIRG X-ray deficit relative to the infrared is observed in both LIRGs that host AGNs and LIRGs that lack AGNs; this point may again call into question whether a population of X-ray binaries (XRBs) could be responsible for the X-ray emission rather than obscured AGNs in these

---

[16] Note that the primary difference between our Figure 2 and Figure 8 in Pfeifle et al. (2019b) is that in the latter, the 12 μm luminosities were calculated by interpolating between the WISE W2 and W3 luminosities, whereas here they are derived directly from the fits to the SED (see Appendix A); thus, the $L_{12\,\mu m}$ values differ accordingly.

Table 5
X-Ray Luminosities for the NuSTAR Nondetected AGNs

System	NuSTAR Observed Luminosity				Chandra Observed Luminosity
	$(10^{42}$ erg s$^{-1})$				$(10^{42}$ erg s$^{-1})$
	3–24 keV	3–10 keV	10–24 keV	2–10 keV	2–10 keV
(1)	(2)	(3)	(4)	(5)	(6)
J0122+0100	<0.656	<0.318	<0.873	<0.409	0.11 ± 0.02
J1221+1137	<2.04	<1.21	<2.66	<1.55	0.09 ± 0.03
J1306+0735	<3.59	<2.55	<3.90	<3.28	0.24 ± 0.04

Note. Luminosities (or upper limits) for the 3–24, 3–10, 10–24, and 2–10 keV energy bands; see Section 3.1.2 and Table 4 for the calculation of the fluxes. Column (1): system name. Columns (2)–(5): NuSTAR luminosities for the 3–24, 3–10, 10–24, and 2–10 keV energy bands. Column (6): observed 2–10 keV Chandra luminosity reported in Pfeifle et al. (2019b), where the luminosities quoted here are the sums of the luminosities of the nuclei in each merger.

mergers. As a simple test, we compared the X-ray and far-infrared luminosities of these sources to the relations presented in Ranalli et al. (2003) and Torres-Albà et al. (2018), where the far-infrared luminosity is expected to accurately trace the star formation rate; we calculated the far-infrared luminosities for these three mergers using the prescription outlined in Section 4.5 of Torres-Albà et al. (2018) after retrieving the 60 and 100 μm flux densities from the IRAS Faint Source Catalog v2.0 (Moshir et al. 1992). We found that the X-ray and far-infrared luminosities of these mergers agree with the relation established by Torres-Albà et al. (2018; Equations (4) and (5) therein were derived for LIRGs that do not show evidence for an AGN in the X-ray or mid-IR); thus, the observed X-ray–to–far-infrared luminosity ratios of these mergers are consistent with those of LIRGs in C-GOALs, which do not host AGNs. This is a puzzling result; at face value, it would suggest that AGNs may not be necessary to explain the X-ray emission in these mergers, but we cannot use that as evidence to rule out the presence of AGNs. It could be a selection effect; 12% (18%) and 10% (14%) of C-GOALS (C-GOALS II) objects are nonmergers or premergers, while another 30% (31%) are early-stage mergers (Torres-Albà et al. 2018). It could be possible that these relations actually vary as a function of merger stage, so the comparison between the late-stage merger LIRGs in this work and the relations derived in Torres-Albà et al. (2018) may not be straightforward. Similarly, Torres-Albà et al. (2018) did not differentiate between LIRGs (log[$L_{8-1000\,\mu m}/L_\odot$] > 11) and ULIRGs (log[$L_{8-1000\,\mu m}/L_\odot$] > 12) when deriving these relations, yet the merger fractions are starkly different when comparing LIRGs and ULIRGs (Kim et al. 2013; log($L_{8-1000\,\mu m}/L_\odot$) > 11.4 is a rough cutoff threshold for mergers dominating LIRGs). Furthermore, this alternative hypothesis is difficult to reconcile with our previous work in Satyapal et al. (2017) and Pfeifle et al. (2019b), as well as the commonplace mid-IR AGN selection criterion (Stern et al. 2012) and the X-ray selection criterion from Iwasawa et al. (2011).

In Satyapal et al. (2017) and Pfeifle et al. (2019b), we used near-IR spectroscopic observations from the Large Binocular Telescope Observatory to estimate the star formation rates (following Kennicutt & Tamblyn 1994) and expected X-ray contribution from XRBs (using the relation from Lehmer et al. 2010, which relates the star formation rate, stellar mass, and X-ray emission for a galaxy and was derived from a sample of local LIRGs). In these calculations, we assumed that all of the Paα emission is due to star formation alone, though in reality, an AGN could contribute to this emission as well; in this way, we placed an upper limit on the expected star formation rates and XRB X-ray contributions. Comparing the observed X-ray

luminosities from Chandra to the expected XRB-driven X-ray emission, we found that our sources are too X-ray luminous to originate from XRBs alone and require an additional source of X-ray emission, i.e., an AGN.

Iwasawa et al. (2011) and Torres-Albà et al. (2018) adopted an X-ray hardness ratio (HR) selection criterion of HR > −0.3 to select X-ray AGNs within C-GOALS I and II. At least one X-ray source in both J0122+0100 and J1306+0735 meets this X-ray selection criterion based upon the reported HRs in Pfeifle et al. (2019b); an additional AGN in both of these mergers just barely misses this cutoff (HR = −0.32 and −0.35). Thus, we have evidence based on X-ray color alone for at least one AGN in each of these mergers, as well as evidence that the X-ray emission cannot be explained solely via star formation based on the near-IR. There were other diagnostics as well that we explored previously, such as the detection of a high-excitation [Si VI] coronal line in both J0122+0100 and J1221+1137, which we take as an unambiguous signature of AGNs. Similarly, J0122+0100 satisfies the WISE AGN color cut of W1 − W2 > 0.8 from Stern et al. (2012) and displays similar AGN colors to other bona fide AGNs within our sample.

In what other ways do these objects compare to the C-GOALS LIRG population? Here we specifically compare against C-GOALS II (Torres-Albà et al. 2018) rather than C-GOALS I (Iwasawa et al. 2011), as the X-ray luminosities in C-GOALS II more closely match those in our sample. In addition to the X-ray–to–far-infrared luminosity correlation, we can also examine the X-ray–to–infrared luminosity ratio, log($L_{2-10\,\mathrm{keV}}/L_{8-1000\,\mu m}$); when considering the total infrared luminosity of the merger system and the combined 2–10 keV X-ray luminosities reported in Pfeifle et al. (2019b), J0122+0100, J1221+1137, and J1306+0735 have a log($L_{2-10\,\mathrm{keV}}/L_{8-1000\,\mu m}$) of −3.9, −4.3, and −3.8. The ratios for J0122+0100 and J1306+0735 suggest that these systems are overluminous (in the 2–10 keV band) relative to the LIRGs in C-GOALS II, including the LIRGs that contain AGNs. However, Iwasawa et al. (2009) noted that the X-ray–to–infrared correlation becomes less clear when systems comprising multiple sources are combined and plotted as a single object, so we instead compute distinct log($L_{2-10\,\mathrm{keV}}/L_{8-1000\,\mu m}$) ratios for each nucleus. We assume the following when assigning fractional contributions to the infrared luminosity: (1) the maximum X-ray luminosities attributable to XRBs in the nuclei of these mergers (reported in Table 7 of Pfeifle et al. 2019b) were derived using near-IR observations and should therefore serve as a proxy for the relative contributions of the nuclei to the near-IR emission, and (2) we can extrapolate this fractional contribution to the total near-IR emission further to the fractional

Table 6
Spectral Fitting Results for J0841+0101

Model	C-stat	d.o.f.	Γ	$N_{\rm H,torus}$ (log[cm^{-2}])	$N_{\rm H,LOS}$ (10^{22} cm^{-2})	R	f_S (%)	T_1 (keV)	T_2 (keV)	Fe Kα EW (keV)
(1)	(2)	(3)	(4)	(5)	(6)	(7)	(8)	(9)	(10)	(11)
PEXRAV	1738.35	1914	$1.9^{+0.3}_{-0.4}$	...	$80.1^{+44.9}_{-52.8}$	$-2.3^{+1.6}_{-6.9}$	$2.7^{+16.1}_{-2.2}$	$0.17^{+0.03}_{-0.06}$	$0.90^{+0.13}_{-0.11}$	$0.26^{+0.15}_{-0.07}$
Borus	1736.80	1914	$2.0^{+0.2}_{-0.2}$	$23.0^{+0.1}_{-0.1}$	121^{+20}_{-18}	...	$0.7^{+0.4}_{-0.3}$	$0.16^{+0.04}_{-0.06}$	$0.90^{+0.14}_{-0.12}$	...

Notes. The J0841+0101 spectral fitting results. Column (1): model choice. Columns (2) and (3): C-stat and degrees of freedom of the model. Columns (4)–(6): photon index, torus column density, and LOS column density. Columns (7) and (8): reflection coefficient and scattered fraction. Columns (9) and (10): temperatures for the two APEC components. Columns (11)–(13): iron Kα line equivalent width.
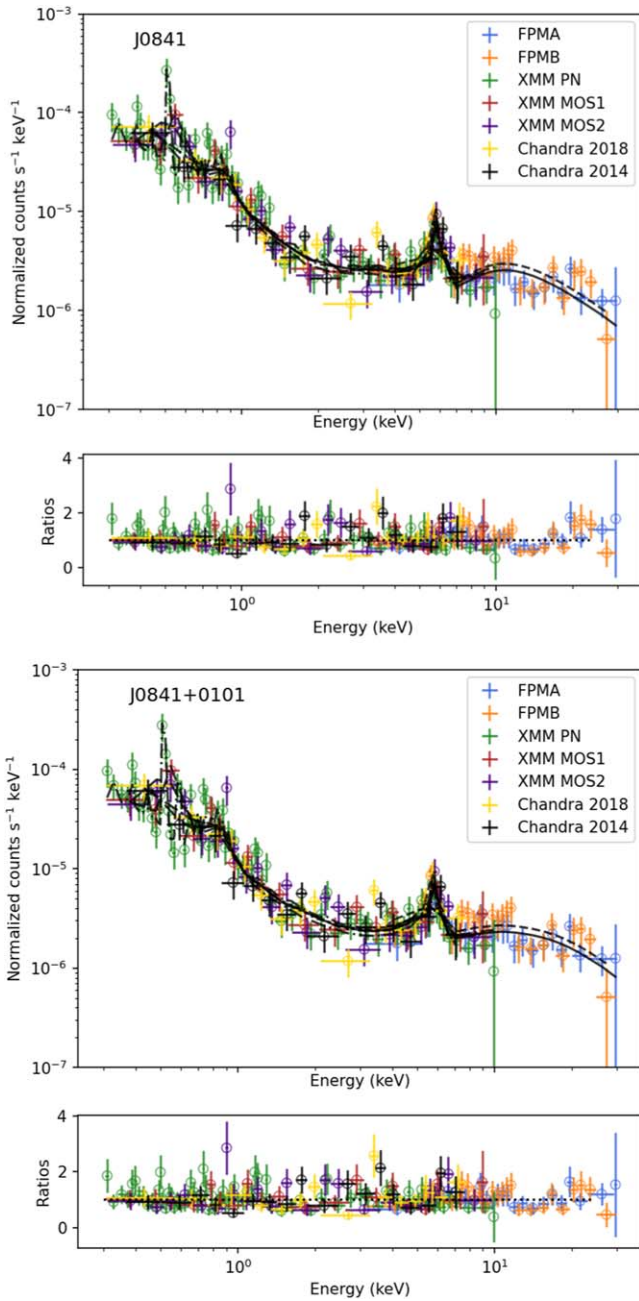
Figure 3. Best-fitting models for J0841+0101. Top: borus model. Bottom: PEXRAV model. Each of these best-fitting models include two soft thermal components in the 0.1–1 keV band, components for reflection and scattered emission, and an absorbed power-law component that accounts for photoelectric absorption and Compton scattering.

contribution to the total infrared luminosity (an admittedly simplistic assumption). Following this prescription, we find $\log(L_{2-10\,{\rm keV}}/L_{8-1000\,\mu{\rm m}})$ ratios of -4.0 and -3.6 in J0122 +0100, -4.2 and -4.8 in J1221+1137, and -3.5, -3.9, and -3.8 for the three sources in J1306+0735. Again, as before, we find that the sources in J0122+0100 and J1306+0735 are either consistent with or overluminous relative to the LIRG population in C-GOALS II when AGNs are included in the LIRG sample $(\log[L_{2-10\,{\rm keV}}/L_{8-1000\,\mu{\rm m}}] = -4.04 \pm 0.48$; see Table 7 in Torres-Albà et al. 2018). These two mergers host X-ray sources that exhibit emission ratios unlike the LIRGs that lack AGNs $(\log[L_{2-10\,{\rm keV}}/L_{8-1000\,\mu{\rm m}}] = -4.18 \pm 0.37$; see Table 7 in Torres-Albà et al. (2018), though they are mostly within the error bounds of the values reported for these ratios in Torres-Albà et al. (2018) due to the scatter in this correlation. The X-ray–to–infrared ratios for J1221+1137, on the other hand, are suspiciously similar to LIRGs that lack AGNs; again, this is difficult to reconcile with the observation of a high-ionization coronal line in one of the nuclei.

Future works will investigate this issue in more depth for the full sample of mid-IR–selected pairs from Satyapal et al. (2017) and Pfeifle et al. (2019b), since the majority of the sample showed similar X-ray deficits and low X-ray luminosities. Based upon the available evidence, our preferred interpretation is that these systems contain AGNs that, given the prevalence of gas and dust in LIRGs, are very likely obscured. However, we cannot rule out that star formation contributes a nonnegligible fraction to the observed X-ray and infrared luminosities; indeed, obscured star-forming regions are also expected in LIRGs, and Pfeifle et al. (2019b) found evidence for soft thermal X-ray components in both J0122+0100 and J1221+1137, implying the presence of star formation–driven emission. If it is the case that star formation contributes significantly to the infrared emission in these galaxy mergers, we could be overpredicting the intrinsic X-ray 2–10 keV luminosities for these sources by using the $L_{2-10\,{\rm keV}}$ versus $L_{12\,\mu{\rm m}}$ relation derived by Asmus et al. (2015) or other similar relations derived for non-LIRG objects. By extension, then, we would be overpredicting the column densities in these AGNs and AGN candidates, since column densities on the order of $\sim 10^{24}$ cm^{-2} may not be needed to explain the X-ray deficit relative to the mid-IR. Unfortunately, the NuSTAR data cannot differentiate between these scenarios.

5.2. The Prevalence of Absorption in Dual AGNs

One long-standing observation among the known population of dual AGNs, as well as dual AGN candidates (at all separations, not just limited to <10 kpc), is the prevalence of

Table 7
Absorbed and Unabsorbed Fluxes for J0841+0101

Model	$F_{2-10 \text{ keV}}$ (10^{-13} erg cm^{-2} s^{-1})		$F_{3-24 \text{ keV}}$ (10^{-13} erg cm^{-2} s^{-1})		$L_{2-10 \text{ keV}}$ (10^{42} erg s^{-1})		$L_{3-24 \text{ keV}}$ (10^{42} erg s^{-1})	
	Obs.	Intr.	Obs.	Intr.	Obs.	Intr.	Obs.	Intr.
(1)	(2)	(3)	(4)	(5)	(6)	(7)	(8)	(9)
PEXRAV	$2.03^{+0.29}_{-0.62}$	9.36	$9.28^{+0.69}_{-2.12}$	18.0	$6.38^{+0.91}_{-1.95}$	29.43	$29.19^{+2.17}_{-6.67}$	56.61
Borus	$2.06^{+0.22}_{-0.94}$	37.8	$4.77^{+0.61}_{-1.95}$	51.6	$6.48^{+0.69}_{-2.96}$	118.9	$15.0^{+1.92}_{-6.13}$	162.3

Notes. The J0841+0101 spectroscopically derived fluxes. Column (1): model choice. Columns (2) and (3): absorbed and intrinsic 2–10 keV flux. Columns (4) and (5): absorbed and intrinsic 3–24 keV flux. Columns (6) and (7): absorbed and intrinsic 2–10 keV luminosity. Columns (8) and (9): absorbed and intrinsic 3–24 keV luminosity.

obscuration along the LOS, where both nuclei are almost ubiquitously found to be obscured by column densities of $N_H > 10^{22}$ cm^{-2}, and at least one (and in some cases both) usually shows higher column densities, on the order of 10^{23}–10^{24} cm^{-2}. Thus, the expectation that mid-IR–selected dual AGNs should be heavily obscured naturally conforms to our present-day paradigm. Clear examples of dual AGNs where both nuclei are Compton-thick include NGC 6240 (Komossa et al. 2003; Nardini 2017) and SWIFT J2028.5+2543 (Koss et al. 2016), while there are several examples of dual AGNs in which one nucleus is Compton-thick while the other is obscured by 10^{23} cm^{-2} (e.g., IRAS 20210+1121 and Mrk 273; Piconcelli et al. 2010; Iwasawa et al. 2018) or 10^{22} cm^{-2} (e.g., Mrk 266; Iwasawa et al. 2020). Others host nuclei where both AGNs are obscured by $>10^{23}$ cm^{-2} (e.g., Mrk 463; Bianchi et al. 2008) or $>10^{22}$ cm^{-2} (e.g., ESO 509-IG066; Guainazzi et al. 2005; Kosec et al. 2017). Large samples of optically selected dual AGNs (confirmed and candidates) typically reveal a mixture of Compton-thin and Compton-thick levels of obscuration (e.g., De Rosa et al. 2018; Hou et al. 2019), and there are some cases where one nucleus is found to be obscured while the other is unobscured (e.g., De Rosa et al. 2018; Hou et al. 2023). There are, however, puzzling cases where one or both nuclei of dual AGNs have been shown to be unobscured, including the Swift-BAT–selected Mrk 739 (Koss et al. 2011; though the flat photon indices are suggestive of more obscured AGNs), J1126+2944 (Comerford et al. 2015; though this is a minor merger with a mass ratio of 460:1, and it is unclear if mergers as minor as these should host heavily obscured AGNs), and SDSS J1108+0659 and SDSS J1146+5110S (which appear to host unobscured and lightly obscured nuclei; Liu et al. 2013). Benítez et al. (2022) recently analyzed archival Chandra data for the Swift-BAT–selected IRAS 05589+2828 (e.g., Koss et al. 2012) and found it consistent with an unobscured Seyfert 1; unfortunately, there were too few counts detected from the companion galaxy (2MASX J06021107+2828382) to examine the column density.

There are a large number of dual AGNs that have been confirmed in the literature that lack constraints on the column densities for one of the nuclei, yet these observations do generally still reveal a significant fraction of obscured AGNs, including Was49b (e.g., Secrest et al. 2017), the triple AGN J0849+1114 (Pfeifle et al. 2019a; Liu et al. 2019), SDSS J140737.17+442856.2 (Ellison et al. 2017; the X-ray-bright nucleus shows only $N_H \sim 2 \times 10^{22}$ cm^{-2}, but the equivalent width of the Fe Kα line, 0.76 keV, would suggest a larger column density), and Arp 299 (constraints are not available for the companion low-luminosity AGN, Pérez-Torres et al. 2010,

but Ptak et al. 2015 found that the X-ray-bright AGN is Compton-thick).

While the general consensus has thus far been that dual AGNs generally show high levels of obscuration, this remains to be confirmed using larger and more statistically complete samples of dual AGNs coupled with soft and hard X-ray observations (in concert with submillimeter observations, which can also trace molecular gas) to constrain the column densities along the LOSs in these systems. Likewise, possible anticorrelations between the projected pair separation and (1) the obscuring column (Guainazzi et al. 2021) and (2) X-ray 2–10 keV flux (Koss et al. 2012) have been reported for dual AGNs but again require larger and statistically complete samples of dual AGNs to confirm these trends. Indeed, the main limitation to understanding the role of obscuration (and other X-ray properties) in dual AGNs (and candidate) environments is the general lack of X-ray spectroscopic information (or multiwavelength information that provides constraints on obscuring columns) for both nuclei in each case and hence column density estimates for each nucleus. For now, a comprehensive examination of the known and candidate populations of dual AGNs in terms of their morphological classes, optical types, selection strategies, and column densities may aid in furthering our understanding of the importance and overall prevalence of obscuration in these systems, though that is beyond the scope of this work; the first literature-complete catalog of dual, binary, and recoiling AGNs (and all candidate systems) is currently in development and slated for release in Q4 2023 and will be a critically important repository of information for the field of dual AGNs going forward (R. W. Pfeifle et al. 2023, in preparation).[17] The AGNs in mergers have been shown to possess higher column densities than isolated control AGNs (e.g., Kocevski et al. 2015), but it is not yet clear whether dual AGNs simply fall within this population or if they show even further enhancements of nuclear obscuration than single AGNs in mergers. Understanding whether dual AGNs are generally more obscured than single AGNs in mergers or isolated AGNs may be important to our understanding of the evolution of dual AGN activation and fueling along the merger sequence.

5.3. Future Prospects for Hard X-Ray Dual AGN Science

Over the last decade, NuSTAR has provided access to the hard X-ray band (3–78 keV), but it has still struggled in the area of dual AGN science because (1) the angular resolution of

---

[17] If you would like to be involved with the development of this catalog, please reach out to the corresponding author of this paper.

NuSTAR has so far been fairly prohibitive for identifying distinct X-ray sources in the imaging for all but the nearest dual AGNs and candidates,[18] and (2) NuSTAR lacks the sensitivity needed to observe many of these systems in a reasonable amount of time. Figure 1 illustrates these two points; of the four dual AGN candidates observed here with NuSTAR, three remain undetected, and while J0841+0101 was robustly detected and spectroscopically examined, the NuSTAR imaging cannot place constraints on the potential number of sources, and the same can be said of the other three systems in our sample (NGC 4922, Mrk 463, and J0849+1114) that have been studied with NuSTAR (Ricci et al. 2017a; Yamada et al. 2018; Pfeifle et al. 2019a). It is likely for these reasons that, aside from a handful systems observed with NuSTAR (e.g., Ptak et al. 2015; Koss et al. 2016; Kosec et al. 2017; Ricci et al. 2017a; Nardini 2017; Iwasawa et al. 2020; this work), hard X-ray (>10 keV) imaging and spectroscopy is not common in the field. Thus, the future of hard X-ray dual AGN research requires better angular and spectral resolution and higher-sensitivity imaging and spectroscopy.

The High Energy X-ray Probe (HEX-P), a current NASA probe-class mission concept, will feature a pair of High Energy Telescopes that would offer broadband (2–80 keV) hard X-ray coverage with a stable point-spread function (PSF) of $\sim16''$ across the field of view, along with a single Low Energy Telescope with an energy range of ~0.2–25 keV and stable PSF of $\sim3.''5$. With $\sim40\times$ better sensitivity in the 10–80 keV band and $12\times$ better angular resolution than NuSTAR, HEX-P could study the X-ray properties of dual AGNs across the merger sequence, from the earliest-stage mergers down to late-stage mergers with nuclear pair separations of $5''$ or lower (R. W. Pfeifle et al. 2023, in preparation). Resolving dual hard X-ray sources in the 10–24 keV imaging with separations on the order of $5''$–$10''$ would be a huge step above what we can currently achieve with NuSTAR (even if, at the closest-resolved separations, the spectra of the two sources are contaminated by one another) and would offer an incredibly clean and efficient means of confirming dual AGNs. Spatially resolved spectroscopy would be another dramatic improvement, enabling constraints on distinct LOS column densities, Fe Kα lines, reflection components, etc., in exquisite detail (R. W. Pfeifle et al. 2023, in preparation) thanks to HEX-P's accessibility to the $\gtrsim6$–30 keV (and higher) energy range and high effective area over that broad range. The HEX-P will struggle in a similar way to NuSTAR as far as resolving the closest-separation dual AGNs ($<5''$–$6''$) in the hard X-ray imaging, but its sensitivity will be a valuable tool for probing the "gross" X-ray properties of the latest-stage merger systems and, in some cases, may allow one to spectrally deconvolve the two sources, as was done with NuSTAR for Mrk 463 (Yamada et al. 2018).

5.4. Star Formation–Driven Thermal Components in Dual AGNs

While obscuration is now a commonly discussed characteristic of dual AGNs and candidates, a seemingly large fraction of these systems with sufficient counts for spectral analysis also show strong soft X-ray emission that is often well fit via soft X-ray thermal components, as we have found in this work for

J0841+0101 and in previous dual AGN candidates (J0122 +0100 and J1221+1137; Pfeifle et al. 2019b). A (nonexhaustive) list of examples from the literature includes NGC 6240 (Komossa et al. 2003), IRAS 20210+1121 (Piconcelli et al. 2010), Mrk 463 (though in this case, the soft X-ray emission was modeled using a series of soft X-ray emission lines; Bianchi et al. 2008), Arp 299 (Ballo et al. 2004), Mrk 266 (Mazzarella et al. 2012), Mrk 739 (Inaba et al. 2022), and SDSS J0945+4238 and SDSS J1038+3921 (De Rosa et al. 2018). Even in cases where soft thermal components are not seen in the X-rays, there is other multiwavelength evidence for starburst activity (like in Mrk 273; Iwasawa et al. 2018) and generally elevated star formation rates. Soft thermal components are commonly found in AGNs (e.g., Winter et al. 2009; Ricci et al. 2017b), so one important question would be, do dual AGNs show soft X-ray thermal components more frequently than isolated AGNs? This should be generally expected, as it has been shown that star formation rates and AGN fractions are expected to increase as a function of decreasing pair separation (e.g., Ellison et al. 2008, 2011), so we should expect that dual AGNs generally show elevated star formation rates and a prevalence of soft X-ray thermal components relative to an isolated control population. A second and related question that we could ask is, do dual AGNs show soft X-ray thermal components more frequently than single AGNs in galaxy mergers? As with understanding the prevalence of obscuration in dual AGNs, we are currently limited by the availability of sensitive X-ray observations for large samples of dual AGNs and candidates. Though beyond the scope of this work, future studies focusing on Chandra, XMM-Newton, and eventually eROSITA observations of dual AGNs should investigate whether soft X-ray thermal components, like obscuration, are fairly ubiquitous in the X-ray spectra of dual AGNs and how the occupational fraction of these spectral features compares to general populations of AGNs in mergers or isolated galaxies.

6. Conclusion

Dual AGNs in late-stage galaxy mergers are predicted to be heavily obscured by gas and dust (Capelo et al. 2015; Blecha et al. 2018), and indeed, many dual AGNs discovered to date (both in late-stage mergers and at larger separations) have shown high absorbing columns along the LOS, on the order of $>10^{23}$–10^{24} cm^{-2} (e.g., Komossa et al. 2003; Bianchi et al. 2008; Piconcelli et al. 2010; Mazzarella et al. 2012; Koss et al. 2016; Secrest et al. 2017; De Rosa et al. 2018; Pfeifle et al. 2019a, 2019b). In this work, we presented new NuSTAR and XMM-Newton observations for a subset of the sample of mid-IR–selected dual AGNs and dual AGN candidates from Satyapal et al. (2017) and Pfeifle et al. (2019b), obtained in an effort to better constrain the column densities along the LOS in these AGNs. We summarize our main conclusions here.

1. Of the four newly observed mid-IR dual AGN candidates, three were not detected by NuSTAR: J0122+0100, J1221 +1137, and J1306+0735. However, J0841+0101 is strongly detected by both XMM-Newton and NuSTAR.

2. The nondetections in J0122+0100, J1221+1137, and J1306+0735 imply that there are no hard X-ray-emitting AGNs in the 10–24 keV band in excess of 1.19×10^{-13}, 2.36×10^{-13}, and 1.23×10^{-13} erg s^{-1} cm^{-2}, respectively, in these systems.

---

[18] But see Ptak et al. (2015) and Kosec et al. (2017) for examples of NuSTAR observations that could resolve the positions of the two putative AGNs.

3. The upper limits on the fluxes for J0122+0100, J1221+1137, and J1306+0735 imply column densities in excess of $\log(N_{\rm H}/{\rm cm}^{-2})$ = 24.9, 24.6, and 24.3 (assuming $C = 0.99$) if we attribute the nondetections to obscuration alone. The 2–10 keV flux upper limits from NuSTAR are consistent with the fluxes derived from Chandra (Pfeifle et al. 2019b). The column density lower limits derived here are also roughly consistent with Pfeifle et al. (2019b), where the differences likely arise due to the difference in the column density estimation method.

4. While we argue that these AGNs are heavily obscured in order to explain the X-ray deficit relative to the mid-IR emission in each merger, we cannot rule out the presence of obscured star-forming regions that contribute significantly to the infrared luminosity. If this were the case, we would be overpredicting the column densities in these AGNs.

5. Our broadband spectroscopic analysis of J0841+0101, combining Chandra, XMM-Newton, and NuSTAR observations, has provided more robust constraints on the X-ray spectral properties of the AGN in this merger. Our best-fitting phenomenological model suggests a total LOS column density of $N_{\rm H} = 80.1^{+44.9}_{-52.8} \times 10^{22}$ cm^{-2}, while our physical torus model suggests a torus obscuring column of $\log(N_{\rm H}/{\rm cm}^{-2}) = 23.0^{+0.1}_{-0.1}$ and an LOS column density of $N_{\rm H} = 121^{+20}_{-18} \times 10^{22}$ cm^{-2}. Our models are also consistent with a power-law photon index of $\Gamma = 1.9^{+0.3}_{-0.4}$ or $2.0^{+0.2}_{-0.2}$ (depending on the model), the presence of two thermal components ($T_1 = 0.17^{+0.03}_{-0.06}$ and $T_2 = 0.90^{+0.13}_{-0.11}$ or $T_1 = 0.16^{+0.04}_{-0.06}$ and $T_2 = 0.90^{+0.14}_{-0.12}$, depending one the model), scattered power-law emission ($0.7^{0.4}_{-0.3}$%–$2.7^{+16.1}_{-2.2}$%, depending on the model), and reflection off of an obscuring medium such as a torus.

Though the majority of the dual AGN candidates studied here were not detected by NuSTAR, our flux upper limits for J0122+0100, J1221+1137, and J1306+0735 and spectroscopic results for J0841+0101, coupled with the previously published results for Mrk 463, NGC 4122, and J0849+1114, are consistent with the picture of WISE-selected dual AGN systems hosting heavily obscured AGNs. Future hard X-ray analyses of dual AGNs and dual AGN candidates, such as those observed here, will benefit greatly from hard X-ray missions with greater sensitivity and angular resolution, like HEX-P.

Appendix A
SED Decomposition

In order to determine the 8–1000 μm IR luminosities of our objects (and, by extension, obtain the intrinsic AGN 12 μm luminosities for use in Section 3.1.3), we fit their SEDs using a custom Python code employed in Powell et al. (2018) for the Swift-BAT AGNs (Koss et al. 2017). In brief, this code convolves the user's choice of SED templates with the system responses corresponding to their data, and the data are fit via weighted nonnegative least-squares, with the weights being the inverse variances of the data. For our data, we combined an AGN template from Fritz et al. (2006), shown in Figure 1 of Hatziminaoglou et al. (2008), with two templates from Chary & Elbaz (2001) corresponding to the lowest and highest IR luminosity star-forming galaxies, which differ primarily in the equivalent widths of their polycyclic aromatic hydrocarbon features and the strength of the IR emission compared with the stellar emission. The AGN template has $W1 - W2/W2 - W3$ synthetic colors of 0.86/2.40, while the low- and high-luminosity star-forming galaxies have corresponding colors of 0.19/1.72 and 0.82/5.67, so our templates have WISE colors typical of AGNs, spiral galaxies, and LIRGs/ULIRGs (e.g., Wright et al. 2010, Figure 12).

We used photometry from the SDSS DR12, the Two Micron All Sky Survey (2MASS; Skrutskie et al. 2006), WISE, and the Infrared Astronomical Satellite (IRAS; Neugebauer et al. 1984)
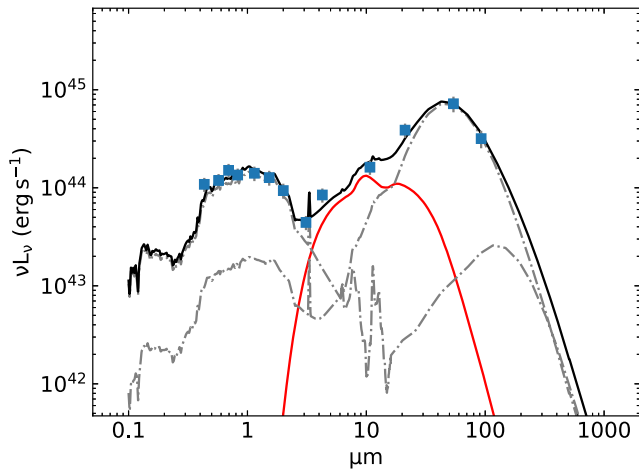
Figure 4. Example of one of our SED fits, SDSS J084905.51+111447.2. The two dashed–dotted gray subcomponents are the star-forming templates, while the red subcomponent is the reddened AGN. The LOS best-fit extinction of the AGN component is $E(B-V) = 16$ mag, indicating that this object is likely Compton-thick with $N_H \sim 1.6 \times 10^{24}$ cm^{-2}. This is within $\sim$3% of the value found in Pfeifle et al. (2019b) using X-ray data from Chandra and NuSTAR. The wavelength scale is rest-frame.

appropriate for extended systems. For SDSS, we used the `modelMag` values, with the exception of the u band, which we exclude due to uncertainties arising from sky-level estimates and the known "red leak"/scattered-light issues with the band.[19] For 2MASS, we use the Extended Source Catalog magnitudes where available and the Point Source Catalog magnitudes otherwise. We do not use the 2MASS data for SDSS J130125.26+291849.5, as the relatively large angular extent of this object means that much of its near-IR emission is below the sky brightness limit of the 2MASS survey, so its near-IR emission is underestimated. For WISE, we use the elliptical `gmag` magnitudes where available and the PSF-fit `mpro` magnitudes otherwise, with the exception of SDSS J130125.26+291849.5, where we use the large-aperture `mag_8` magnitudes. For sources with IR flux densities in either the IRAS Point Source Catalog (PSC) or the IRAS Faint Source Catalog, we additionally use the 60 and 100 μm flux densities, preferentially from the PSC. To convert to the AB system, we added 0.02 mag to the SDSS z band[20] and used the 2MASS Vega/AB offsets available in TOPCAT[21] and the standard Vega/AB offsets listed in the WISE documentation.[22] Finally, we corrected the g through W2 magnitudes for Galactic dust extinction using $E(B-V)$ values following Schlafly & Finkbeiner (2011). To account for systematic errors arising due to differences of aperture and flux calibration between the photometry catalogs, as well as differences between the SED templates and the true object SED, we fit

Table 8
SED Fitting Results

SDSS	E_{B-V}^{AGN}	$\log\left(\frac{L_{12\,\mu m}^{AGN}}{\mathrm{erg\ s}^{-1}}\right)$	$\log\left(\frac{L_{8-1000\,\mu m}}{L_\odot}\right)$
J0122+0100	$0.0^{+11.0}_{-0.0}$	$43.1^{+0.7}_{-0.1}$	$11.3^{+0.1}_{-0.3}$
J0841+0101	$15.0^{+4.0}_{-13.1}$	$44.7^{+0.2}_{-0.8}$	$11.7^{+0.3}_{-0.6}$
J0849+1114	$16.0^{+5.0}_{-5.0}$	$44.2^{+0.2}_{-0.2}$	$11.4^{+0.1}_{-0.1}$
J0859+1310	$0.7^{+7.6}_{-0.3}$	$42.6^{+0.3}_{-0.2}$	$10.2^{+0.1}_{-0.2}$
J0905+3747	$1.9^{+5.0}_{-1.9}$	$43.1^{+0.3}_{-0.3}$	$11.2^{+0.1}_{-0.2}$
J1036+0221	$11.0^{+7.0}_{-11.0}$	$43.8^{+0.3}_{-0.7}$	$11.7^{+0.1}_{-0.2}$
J1045+3519	$0.0^{+11.0}_{-0.0}$	$43.2^{+0.6}_{-0.2}$	$11.6^{+0.1}_{-0.2}$
J1126+1913	$7.5^{+11.5}_{-7.5}$	$43.4^{+0.5}_{-0.8}$	$11.5^{+0.1}_{-0.3}$
J1147+0945	$0.5^{+0.2}_{-0.3}$	$43.6^{+0.1}_{-0.1}$	$10.6^{+0.1}_{-0.3}$
J1159+5320	$8.2^{+1.5}_{-1.6}$	$43.0^{+0.0}_{-0.1}$	$10.1^{+0.0}_{-0.1}$
J1221+1137	$0.0^{+12.0}_{-0.0}$	$43.2^{+0.6}_{-0.3}$	$11.7^{+0.1}_{-0.1}$
J1301+2918	$0.7^{+4.3}_{-0.1}$	$43.2^{+0.2}_{-0.1}$	$11.3^{+0.0}_{-0.1}$
J1306+0735	$0.0^{+22.0}_{-0.0}$	$43.1^{+1.1}_{-0.1}$	$11.6^{+0.0}_{-0.1}$
J1356+1822	$3.6^{+1.4}_{-3.6}$	$44.8^{+0.1}_{-0.1}$	$11.4^{+0.1}_{-0.1}$
J2356−1016	$0.0^{+4.5}_{-0.0}$	$44.0^{+0.3}_{-0.1}$	$11.5^{+0.1}_{-0.2}$

Notes. Here $L_{12\,\mu m}^{AGN}$ is the intrinsic rest-frame 12 μm monochromatic luminosity of the AGN component, and $L_{8-1000\,\mu m}$ is the integrated 8–1000 μm luminosity of the star-forming templates. The confidence intervals are 5%–95%. The AGN reddening of $E(B-V) = 1$ approximately corresponds to $N_H = 10^{23}$ cm^{-2} (Maiolino et al. 2001).

each object iteratively, increasing the formal photometric errors in quadrature until the reduced χ^2 of the fit became unity. At each iteration, we fit the AGN component along a grid of $E(B-V)$ values ranging from 0.0 to 50, which corresponds to a neutral hydrogen column density range from zero to $\sim$5 $\times$ 10^{24} cm^{-2} (Maiolino et al. 2001). We used the Gordon & Clayton (1998) extinction curve for UV wavelengths and the Cardelli et al. (1989) extinction curve otherwise. To estimate the confidence intervals, we fit each object 10^4 times, at each iteration drawing a permutation of the magnitudes using the adjusted uncertainties. We find that our systems have 8–1000 μm luminosities from star formation between 1.2×10^{10} and $5.3 \times 10^{11}\,L_\odot$, with a mean value of $2.7 \times 10^{11}\,L_\odot$, and 80% of our systems are above $10^{11}\,L_\odot$, placing them predominantly in the class of LIRGs. We show an example of one of our SED fits in Figure 4 and provide the 8–1000 and 12 μm luminosities in Table 8.

Appendix B
Poorer Spectral Fitting Results for J0841+0101

For clarity, we include in Table 9 the results of the poorer spectral fits described in Section 3.2.

---

[19] https://www.sdss.org/dr12/imaging/caveats/
[20] https://www.sdss.org/dr12/algorithms/fluxcal/#SDSStoAB
[21] Version 4.6-1; http://www.star.bris.ac.uk/~mbt/topcat.
[22] http://wise2.ipac.caltech.edu/docs/release/allsky/expsup/sec4_4h.html#conv2ab

Table 9
Poorer Spectral Fitting Results for J0841+0101

Model	C-stat	d.o.f.	Γ	$N_{\rm H,torus}$ (log[cm^2])	$N_{\rm H,LOS}$ (10^{22} cm^{-2})	R	$f_{\rm S}$ (%)	T_1 (keV)	T_2 (keV)
(1)	(2)	(3)	(4)	(5)	(6)	(7)	(8)	(9)	(10)
PEXRAV	2156.57	1918	$1.5^{+0.04}_{-0.04}$	...	NC	$-10.0^{+0.2}_{+10}$	NC	...	...
PEXRAV	1943.95	1917	$1.4^{+0.01}_{-1.4}$	...	NC	$-10.0^{+0.2}_{\rm NC}$	...	$0.21^{+0.02}_{-0.02}$	...
PEXRAV	1792.82	1915	$2.4^{\rm NC}_{-0.1}$	...	$133.0^{+26.1}_{-22.9}$	$-0.6^{+0.3}_{-0.5}$	...	$0.19^{+0.02}_{-0.03}$	$1.05^{+0.13}_{-0.12}$
PEXRAV	1788.95	1916	$2.2^{\rm NC}_{-0.3}$	...	$91.6^{+27.5}_{-28.3}$	$-0.8^{+0.4}_{-0.9}$	$1.0^{+2.1}_{-0.7}$	$0.22^{+0.02}_{-0.03}$	...
PEXRAV	1759.23	1914	$2.0^{+0.3}_{-0.3}$	...	$86.1^{+33.4}_{-34.3}$	$-1.4^{+0.8}_{-2.2}$	$1.3^{+3.5}_{-0.9}$	$0.17^{+0.03}_{-0.06}$	$0.91^{+0.13}_{-0.12}$
Borus	2277.74	1916	$1.4^{+0.0}_{\rm NC}$	$22.1^{+0.1}_{-0.1}$	...	...	...	$0.27^{+0.02}_{-0.01}$	...
Borus	1861.91	1914	$1.4^{+0.031}_{\rm NC}$	$23.4^{+0.1}_{-0.1}$	...	...	...	$0.22^{+0.02}_{-0.01}$	$2.00^{\rm NC}_{-0.04}$
Borus	1878.45	1917	$2.2^{+0.1}_{-0.03}$	$23.8^{+0.1}_{-0.05}$	...	...	$2.14^{+0.4}_{-0.3}$	...	...
Borus	1788.86	1915	$1.5^{+0.1}_{\rm NC}$	$23.7^{+0.1}_{-0.1}$	...	...	$8.75^{+2.4}_{-2.8}$	$0.22^{+0.02}_{-0.02}$	...
Borus	1755.74	1913	$1.4^{+0.1}_{-1.4}$	$23.6^{+0.1}_{-0.1}$	...	...	$9.06^{+1.8}_{-2.1}$	$0.17^{+0.03}_{-0.17}$	$0.90^{+0.13}_{-0.14}$

Note. The J0841+0101 spectral fitting results from other model permutations. Column (1): model choice. Columns (2) and (3): C-stat and degrees of freedom of the model. Columns (4)–(6): photon index, torus column density, and LOS column density. Columns (7) and (8): reflection coefficient and scattered fraction. Columns (9) and (10): temperatures for the two APEC components. Here NC indicates that the value was unphysical and/or not constrained during fitting.

ORCID iDs

Ryan W. Pfeifle ⓘ https://orcid.org/0000-0001-8640-8522
Shobita Satyapal ⓘ https://orcid.org/0000-0003-2277-2354
Claudio Ricci ⓘ https://orcid.org/0000-0001-5231-2645
Nathan J. Secrest ⓘ https://orcid.org/0000-0002-4902-8077
Mario Gliozzi ⓘ https://orcid.org/0000-0002-8818-9009
Laura Blecha ⓘ https://orcid.org/0000-0002-2183-1087
Barry Rothberg ⓘ https://orcid.org/0000-0003-2283-2185

References

Abazajian, K. N., Adelman-McCarthy, J. K., Agüeros, M. A., et al. 2009, ApJS, 182, 543
Arnaud, K. A. 1996, in ASP Conf. Ser. 101, Astronomical Data Analysis Software and Systems V, ed. G. H. Jacoby & J. Barnes (San Francisco, CA: ASP), 17
Asmus, D., Gandhi, P., Hönig, S. F., Smette, A., & Duschl, W. J. 2015, MNRAS, 454, 766
Astropy Collaboration, Price-Whelan, A. M., Sipőcz, B. M., et al. 2018, AJ, 156, 123
Astropy Collaboration, Robitaille, T. P., Tollerud, E. J., et al. 2013, A&A, 558, A33
Ballo, L., Braito, V., Della Ceca, R., et al. 2004, ApJ, 600, 634
Baloković, M., Brightman, M., Harrison, F. A., et al. 2018, ApJ, 854, 42
Barnes, J. E., & Hernquist, L. 1996, ApJ, 471, 115
Barnes, J. E., & Hernquist, L. E. 1991, ApJL, 370, L65
Benítez, E., Jiménez-Bailón, E., Negrete, C. A., et al. 2022, MNRAS, 516, 5270
Bianchi, S., Chiaberge, M., Piconcelli, E., Guainazzi, M., & Matt, G. 2008, MNRAS, 386, 105
Blecha, L., Snyder, G. F., Satyapal, S., & Ellison, S. L. 2018, MNRAS, 478, 3056
Brightman, M., Nandra, K., Salvato, M., et al. 2014, MNRAS, 443, 1999
Capelo, P. R., Dotti, M., Volonteri, M., et al. 2017, MNRAS, 469, 4437
Capelo, P. R., Volonteri, M., Dotti, M., et al. 2015, MNRAS, 447, 2123
Cardelli, J. A., Clayton, G. C., & Mathis, J. S. 1989, ApJ, 345, 245
Cash, W. 1979, ApJ, 228, 939
Chary, R., & Elbaz, D. 2001, ApJ, 556, 562
Comerford, J. M., Gerke, B. F., Stern, D., et al. 2012, ApJ, 753, 42
Comerford, J. M., Pooley, D., Barrows, R. S., et al. 2015, ApJ, 806, 219
Comerford, J. M., Pooley, D., Gerke, B. F., & Madejski, G. M. 2011, ApJL, 737, L19
Darg, D. W., Kaviraj, S., Lintott, C. J., et al. 2010, MNRAS, 401, 1043
De Rosa, A., Vignali, C., Husemann, B., et al. 2018, MNRAS, 480, 1639
Ellison, S. L., Patton, D. R., Mendel, J. T., & Scudder, J. M. 2011, MNRAS, 418, 2043
Ellison, S. L., Patton, D. R., Simard, L., & McConnachie, A. W. 2008, AJ, 135, 1877

Ellison, S. L., Secrest, N. J., Mendel, J. T., Satyapal, S., & Simard, L. 2017, MNRAS, 470, L49
Ferrarese, L., & Merritt, D. 2000, ApJL, 539, L9
Foord, A., Gültekin, K., Nevin, R., et al. 2020, ApJ, 892, 29
Fritz, J., Franceschini, A., & Hatziminaoglou, E. 2006, MNRAS, 366, 767
Fruscione, A., McDowell, J. C., Allen, G. E., et al. 2006, Proc. SPIE, 6270, 62701V
Gabriel, C., Denby, M., Fyfe, D. J., et al. 2004, in ASP Conf. Ser. 314, Astronomical Data Analysis Software and Systems (ADASS) XIII, ed. F. Ochsenbein, M. G. Allen, & D. Egret (San Francisco, CA: ASP), 759
Gebhardt, K., Bender, R., Bower, G., et al. 2000, ApJL, 539, L13
Gordon, K. D., & Clayton, G. C. 1998, ApJ, 500, 816
Guainazzi, M., De Rosa, A., Bianchi, S., et al. 2021, MNRAS, 504, 393
Guainazzi, M., Piconcelli, E., Jiménez-Bailón, E., & Matt, G. 2005, A&A, 429, L9
Gültekin, K., Richstone, D. O., Gebhardt, K., et al. 2009, ApJ, 698, 198
Harris, C. R., Millman, K. J., van der Walt, S. J., et al. 2020, Natur, 585, 357
Harrison, F. A., Craig, W. W., Christensen, F. E., et al. 2013, ApJ, 770, 103
Hatziminaoglou, E., Fritz, J., Franceschini, A., et al. 2008, MNRAS, 386, 1252
Hopkins, P. F., Hernquist, L., Cox, T. J., & Kereš, D. 2008, ApJS, 175, 356
Hopkins, P. F., Hernquist, L., Cox, T. J., et al. 2006, ApJS, 163, 1
Hou, M., Li, Z., Liu, X., et al. 2023, ApJ, 943, 50
Hou, M., Liu, X., Guo, H., et al. 2019, ApJ, 882, 41
Hunter, J. D. 2007, CSE, 9, 90
Ichikawa, K., Ricci, C., Ueda, Y., et al. 2017, ApJ, 835, 74
Ichikawa, K., Ricci, C., Ueda, Y., et al. 2019, ApJ, 870, 31
Inaba, K., Ueda, Y., Yamada, S., et al. 2022, ApJ, 939, 88
Iwasawa, K., Ricci, C., Privon, G. C., et al. 2020, A&A, 640, A95
Iwasawa, K., Sanders, D. B., Evans, A. S., et al. 2009, ApJL, 695, L103
Iwasawa, K., Sanders, D. B., Teng, S. H., et al. 2011, A&A, 529, A106
Iwasawa, K., V, U., Mazzarella, J. M., et al. 2018, A&A, 611, A71
Joye, W. A., & Mandel, E. 2003, in ASP Conf. Ser. 295, Astronomical Data Analysis Software and Systems XII, ed. H. E. Payne, R. I. Jedrzejewski, & R. N. Hook (San Francisco, CA: ASP), 489
Kennicutt, R. C., Jr., Tamblyn, P., & Congdon, C. E. 1994, ApJ, 435, 22
Kim, D. C., Evans, A. S., Vavilkin, T., et al. 2013, ApJ, 768, 102
Kocevski, D. D., Brightman, M., Nandra, K., et al. 2015, ApJ, 814, 104
Komossa, S., Burwitz, V., Hasinger, G., et al. 2003, ApJL, 582, L15
Kosec, P., Brightman, M., Stern, D., et al. 2017, ApJ, 850, 168
Koss, M., Mushotzky, R., Treister, E., et al. 2011, ApJL, 735, L42
Koss, M., Mushotzky, R., Treister, E., et al. 2012, ApJL, 746, L22
Koss, M., Trakhtenbrot, B., Ricci, C., et al. 2017, ApJ, 850, 74
Koss, M. J., Blecha, L., Bernhard, P., et al. 2018, Natur, 563, 214
Koss, M. J., Glidden, A., Baloković, M., et al. 2016, ApJL, 824, L4
Kraft, R. P., Burrows, D. N., & Nousek, J. A. 1991, ApJ, 374, 344
Lansbury, G. B., Alexander, D. M., Del Moro, A., et al. 2014, ApJ, 785, 17
Lansbury, G. B., Gandhi, P., Alexander, D. M., et al. 2015, ApJ, 809, 115
Lansbury, G. B., Stern, D., Aird, J., et al. 2017, ApJ, 836, 99
Lanzuisi, G., Civano, F., Marchesi, S., et al. 2018, MNRAS, 480, 2578
Lehmer, B. D., Alexander, D. M., Bauer, F. E., et al. 2010, ApJ, 724, 559
Lintott, C. J., Schawinski, K., Slosar, A., et al. 2008, MNRAS, 389, 1179

Liu, X., Civano, F., Shen, Y., et al. 2013, ApJ, 762, 110
Liu, X., Hou, M., Li, Z., et al. 2019, ApJ, 887, 90
Liu, X., Shen, Y., Strauss, M. A., & Greene, J. E. 2010, ApJ, 708, 427
Liu, X., Shen, Y., Strauss, M. A., & Hao, L. 2011, ApJ, 737, 101
Maiolino, R., Marconi, A., Salvati, M., et al. 2001, A&A, 365, 28
Marchesi, S., Ajello, M., Marcotulli, L., et al. 2018, ApJ, 854, 49
Mazzarella, J. M., Iwasawa, K., Vavilkin, T., et al. 2012, AJ, 144, 125
McKinney, W. 2010, in Proc. 9th Python in Science Conf., ed.
    S. van der Walt & J. Millman, 56
Mihos, J. C., & Hernquist, L. 1996, ApJ, 464, 641
Moshir, M., Kopman, G., & Conrow, T. A. O. 1992, IRAS Faint Source
    Survey, Explanatory Supplement version 2 (Pasadena, CA: California
    Institute of Technology)
Müller-Sánchez, F., Comerford, J. M., Nevin, R., et al. 2015, ApJ, 813, 103
Mushotzky, R. F., Done, C., & Pounds, K. A. 1993, ARA&A, 31, 717
Nasa High Energy Astrophysics Science Archive Research Center 2014,
    HEAsoft: Unified Release of FTOOLS and XANADU, Astrophysics Source
    Code Library, ascl:1408.004
Nardini, E. 2017, MNRAS, 471, 3483
Neugebauer, G., Habing, H. J., van Duinen, R., et al. 1984, ApJL, 278, L1
Oliphant, T. E. 2006, A Guide to NumPy, Vol. 1 (USA: Trelgol Publishing),
    https://web.mit.edu/dvp/Public/numpybook.pdf
Pérez-Torres, M. A., Alberdi, A., Romero-Cañizales, C., & Bondi, M. 2010,
    A&A, 519, L5
Perri, M., Puccetti, S., Spagnuolo, N., et al. 2021, The NuSTAR Data Analysis
    Software Guide, Version 1.9.7, ASI Space Science Data Center and
    California Institute of Technology, https://heasarc.gsfc.nasa.gov/docs/
    nustar/analysis/nustar_swguide.pdf
Pfeifle, R. W., Ricci, C., Boorman, P. G., et al. 2022, ApJS, 261, 3
Pfeifle, R. W., Satyapal, S., Manzano-King, C., et al. 2019a, ApJ, 883, 167
Pfeifle, R. W., Satyapal, S., Ricci, C., et al. 2023, ApJ, 943, 109
Pfeifle, R. W., Satyapal, S., Secrest, N. J., et al. 2019b, ApJ, 875, 117
Piconcelli, E., Vignali, C., Bianchi, S., et al. 2010, ApJL, 722, L147
Powell, M. C., Cappelluti, N., Urry, C. M., et al. 2018, ApJ, 858, 110
Ptak, A., Hornschemeier, A., Zezas, A., et al. 2015, ApJ, 800, 104
Ranalli, P., Comastri, A., & Setti, G. 2003, A&A, 399, 39
Ricci, C., Bauer, F. E., Treister, E., et al. 2017a, MNRAS, 468, 1273
Ricci, C., Privon, G. C., Pfeifle, R. W., et al. 2021, MNRAS, 506, 5935
Ricci, C., Trakhtenbrot, B., Koss, M. J., et al. 2017b, ApJS, 233, 17
Ricci, C., Ueda, Y., Koss, M. J., et al. 2015, ApJL, 815, L13
Robitaille, T., & Bressert, E. 2012, APLpy: Astronomical Plotting Library in
    Python, Astrophysics Source Code Library, ascl:1208.017
Satyapal, S., Secrest, N. J., McAlpine, W., et al. 2014, ApJ, 784, 113
Satyapal, S., Secrest, N. J., Ricci, C., et al. 2017, ApJ, 848, 126
Schlafly, E. F., & Finkbeiner, D. P. 2011, ApJ, 737, 103
Secrest, N. J., Schmitt, H. R., Blecha, L., Rothberg, B., & Fischer, J. 2017,
    ApJ, 836, 183
Skrutskie, M. F., Cutri, R. M., Stiening, R., et al. 2006, AJ, 131, 1163
Smith, K. L., Shields, G. A., Bonning, E. W., et al. 2010, ApJ, 716, 866
Stern, D. 2015, ApJ, 807, 129
Stern, D., Assef, R. J., Benford, D. J., et al. 2012, ApJ, 753, 30
Taylor, M. B. 2005, in ASP Conf. Ser. 347, Astronomical Data Analysis
    Software and Systems XIV, ed. P. Shopbell, M. Britton, & R. Ebert (San
    Francisco, CA: ASP), 29
Torres-Albà, N., Iwasawa, K., Díaz-Santos, T., et al. 2018, A&A, 620,
    A140
Tozzi, P., Gilli, R., Mainieri, V., et al. 2006, A&A, 451, 457
van der Walt, S., Colbert, S. C., & Varoquaux, G. 2011, CSE, 13, 22
Van Wassenhove, S., Volonteri, M., Mayer, L., et al. 2012, ApJL, 748, L7
Virtanen, P., Gommers, R., Oliphant, T. E., et al. 2020, NatMe, 748, L7
Wang, J.-M., Chen, Y.-M., Hu, C., et al. 2009, ApJL, 705, L76
Willingale, R., Starling, R. L. C., Beardmore, A. P., Tanvir, N. R., &
    O'Brien, P. T. 2013, MNRAS, 431, 394
Wright, E. L., Eisenhardt, P. R. M., Mainzer, A. K., et al. 2010, AJ, 140, 1868
Winter, L. M., Mushotzky, R. F., Reynolds, C. S., & Tueller, J. 2009, ApJ,
    690, 1322
Wright, E. L., Eisenhardt, P. R. M., Mainzer, A. K., et al. 2019, AllWISE
    Source Catalog, IPAC, doi:10.26131/IRSA1
Yamada, S., Ueda, Y., Oda, S., et al. 2018, ApJ, 858, 106
Yamada, S., Ueda, Y., Tanimoto, A., et al. 2021, ApJS, 257, 61